MEGARA-IFU detection of extended He II λ4686 nebular emission in the central region of NGC 1569 and its ionization budget

Y. D. Mayya,[1]⋆ E. Carrasco,[1] V. M. A. Gómez-González,[2] J. Zaragoza-Cardiel ●,[1,3] A. Gil de Paz ●,[4]

P. A. Ovando,[1] M. Sánchez-Cruces ●,[5] L. Lomelí-Núñez ●,[1] L. Rodríguez-Merino,[1]

D. Rosa-González ●,[1] S. Silich,[1] G. Tenorio-Tagle,[1] G. Bruzual,[2] S. Charlot,[6] R. Terlevich,[1,7]

E. Terlevich,[1] O. Vega,[1] J. Gallego,[4] J. Iglesias-Páramo,[8,9] A. Castillo-Morales,[4] M. L. García-Vargas ●,[10]

P. Gómez-Alvarez,[10] S. Pascual[4] and A. Pérez-Calpena[10]

[1]*Instituto Nacional de Astrofísica, Óptica y Electrónica, Luis Enrique Erro 1, Tonantzintla 72840, Puebla, Mexico*
[2]*Instituto de Radioastronomía y Astrofísica, UNAM Campus Morelia, Apartado Postal 3-72, 58090 Morelia, Michoacán, Mexico*
[3]*Consejo Nacional de Ciencia y Tecnología, Av. Insurgentes Sur 1582, 03940 Mexico City, Mexico*
[4]*Departamento de Física de la Tierra y Astrofísica, Instituto de Física de Partículas y del Cosmos (IPARCOS), Fac. CC. Físicas, Universidad Complutense de Madrid, Plaza de las Ciencias, 1, E-28040 Madrid, Spain*
[5]*Aix Marseille Université, CNRS, LAM, 13388 Marseille Cedex 13, France*
[6]*Institut d'Astrophysique de Paris, Sorbonne Université, CNRS, UMR7095, F-75014 Paris, France*
[7]*Institute of Astronomy, University of Cambridge, Cambridge CB3 0HA, UK*
[8]*Instituto de Astrofísica de Andalucía, IAA-CSIC, Glorieta de la Astronomía s/n, E-18008 Granada, Spain*
[9]*Estación Experimental de Zonas Áridas, CSIC, Carretera de Sacramento s/n, E-04120 Almería, Spain*
[10]*FRACTAL S.L.N.E., Calle Tulipán 2, portal 13, 1A, E-28231 Las Rozas de Madrid, Spain*

ABSTRACT

We here report the detection of extended He II λ4686 nebular emission in the central region of NGC 1569 using the integral field spectrograph MEGARA at the 10.4 m Gran Telescopio Canarias. The observations cover a field of view (FoV) of 12.5 arcsec × 11.3 arcsec at a seeing-limited spatial resolution of ∼15 pc and at a spectral resolution of $R = 6000$ in the wavelength range 4330–5200 Å. The emission extends over a semicircular arc of ∼40 pc width and ∼150 pc diameter around the superstar cluster A (SSC-A). The A_V derived using Balmer decrement varies from the Galactic value of 1.6 mag to a maximum of ∼4.5 mag, with a mean value of 2.65 ± 0.60 mag. We infer 124 ± 11 Wolf–Rayet (WR) stars in SSC-A using the He II λ4686 broad feature and $A_V = 2.3$ mag. The He$^+$ ionizing photon rate from these WR stars is sufficient to explain the luminosity of the He II nebula. The observationally determined total He$^+$ and H^0 ionizing photon rates, their ratio, and the observed number of WR stars in SSC-A are all consistent with the predictions of simple stellar population models at an age of 4.0 ± 0.5 Myr and a mass of $(5.5 \pm 0.5) \times 10^5$ M$_\odot$. Our observations reinforce the absence of WR stars in SSC-B, the second most massive cluster in the FoV. None of the other locations in our FoV where He II λ4686 emission has been reported from narrow-band imaging observations contain WR stars.

Key words: galaxies: individual (NGC 1569) – galaxies: star clusters – stars: emission line.

1 INTRODUCTION

The availability of large telescopes equipped with integral field spectrographs has enabled the creation of maps of He II λ4686 nebular emission in nearby star-forming galaxies (e.g. Kehrig et al. 2015, 2018). Given that only photons shortward of 228 Å (54 eV) can doubly ionize helium, the He II λ4686 line provides a ground-based tool to trace the hard part of the ultraviolet (UV) spectrum. High-mass stars, especially during their short-duration Wolf–Rayet (WR) phase, are the most common sources that emit these hard UV photons (Schaerer 1996). The UV flux emerging from a starburst

region depends both on the hardness of the UV spectrum of WR stars as well as on the number of WR stars present. Because of the presence of an expanding atmosphere, models incorporating specialized line-blanketing treatment are required in order to quantitatively predict the flux of hard UV photons emitted by the WR stars. The emergent spectra in models incorporating such treatment (e.g. Hillier & Miller 1998; Gräfener, Koesterke & Hamann 2002) are found to be softer as compared to earlier models that did not take into account opacities from metals (Schmutz, Leitherer & Gruenwald 1992). On the other hand, the number of WR stars and the duration of the WR phase in a starburst region depend on metallicity (e.g. Maeder & Meynet 1989; Schaller et al. 1992; Bressan, Chiosi & Fagotto 1994; Chen et al. 2015), stellar rotation (Meynet & Maeder 2005), and the stellar multiplicity (Eldridge et al. 2017). The calculated rate of He$^+$

⋆ E-mail: ydm@inaoep.mx

ionizing photons at different metallicities depends critically on the mass-loss recipes used during massive star evolution. The general trend from the different set of currently available codes is a decrease in the expected luminosity of the He II λ4686 line with decreasing metallicity.

The spectra from Sloan Digital Sky Survey (SDSS) have enabled the detection of the relatively faint He II λ4686 line in large samples of star-forming galaxies (e.g. Shirazi & Brinchmann 2012). These studies find that the observed He II λ4686/Hβ intensity ratio does not drop at low metallicities. In fact, recent studies find the ratio to be increasing as the metallicity decreases (Schaerer, Fragos & Izotov 2019). Furthermore, these low-metallicity He II λ4686-emitting galaxies often show only a weak or no evidence of the presence of WR stars (Shirazi & Brinchmann 2012). Thus, questions have been raised on the WR stars as the sole source of ionization of He$^+$ (Plat et al. 2019). Alternative mechanisms such as hard radiation from high-mass stars in binaries (Eldridge et al. 2017), shocks from supernova remnants (Garnett et al. 1991; Dopita & Sutherland 1996), and high-mass X-ray binaries (HMXBs; Schaerer et al. 2019; Kojima et al. 2020) are often invoked. Nearby low-metallicity systems offer an opportunity to address the He$^+$ ionization problem by enabling study of individual star-forming knots. In a detailed study of the metal-poor ($Z = 3$–4 per cent Z$_\odot$) galaxy SBS 0335−052E using MUSE, Kehrig et al. (2018) discard WR stars as the source of ionization and instead propose rotating metal-free stars or a binary population with $Z = 10^{-5}$ and an extremely top-heavy initial mass function (IMF) as the only plausible way of getting around the problem of the ionization budget. In a recent study, Schaerer et al. (2019) find that the observed He II λ4686 intensity in metal-poor star-forming galaxies can be naturally reproduced if the bulk of the He$^+$ ionizing photons is emitted by the HMXB, whose number is found to increase with decreasing metallicity. X-ray binaries in a cluster appear only after the death of the most massive stars, and hence this scenario cannot explain the He$^+$ ionization in young systems [Hβ equivalent widths (EWs) $\geq$ 200 Å], as illustrated by Plat et al. (2019).

A detailed analysis of the He II ionization budget problem has been carried out only in a handful of extreme metal-poor galaxies (e.g. Kehrig et al. 2011, 2018). The lack of observational data of individual massive stars at these low metallicities makes the predictions of population synthesis calculations heavily dependent on the theoretical assumptions. On the other hand, model calculations have been better calibrated at the LMC and solar metallicities. However, its detection requires sensitive observations, specially aimed at detecting faint emission lines. The newly available spectrograph MEGARA at the 10.4 m Gran Telescopio Canarias (GTC) equipped with Integral Field Unit (IFU) at a spectral resolution of ∼6000 has the capability of detecting and mapping the faint emission lines from extragalactic nebulae (Gil de Paz et al. 2020). In order to exploit this capability, we carried out MEGARA observations of NGC 1569, a dwarf galaxy with a gas-phase oxygen abundance close to that of the LMC [12 + log (O/H) = 8.19; Kobulnicky & Skillman 1997]. We mapped its central region, which is known to have extended Hα emission (Hodge 1974; Waller 1991; Hunter, Hawley & Gallagher 1993). Throughout this study, we use a distance of 3.1 Mpc, measured using *Hubble Space Telescope* (*HST*) observations of the tip of the red giant branch (RGB; Grocholski et al. 2012). This distance is ∼10 per cent smaller than that obtained by Grocholski et al. (2008) using an earlier analysis of the same data set, but is still considerably higher than the 2.2 Mpc distance (Israel 1988) that was being routinely used in studies prior to the Grocholski et al. (2008) work.

NGC 1569 is among the nearest galaxies that harbours young superstellar clusters (SSCs) that are as massive as the Galactic globular clusters. Its most massive SSCs, called A and B, are estimated to have dynamical masses of 4.1×10^5 M$_\odot$ (Ho & Filippenko 1996) and 6.2×10^5 M$_\odot$ (Larsen et al. 2008), respectively [after rescaling the masses to the currently used distance of 3.1 Mpc for this galaxy from Grocholski et al. (2012)]. These two SSCs are at the high-mass end of a population of around 50 SSCs, whose ages range from a few million to several hundred million years (Hunter et al. 2000). The Hα morphology of the galaxy is dominated by H II regions (Waller 1991), large-scale shells, and superbubbles (Hunter et al. 1993; Westmoquette et al. 2008), with the brightest H II region in this galaxy associated with the star-forming complex surrounding cluster 10 of Hunter et al. (2000) that lies 105 pc (7 arcsec) to the east of superstar cluster A (SSC-A), and is outside our field of view (FoV). Extended X-ray emission is detected in the galaxy, most of which coincides with the Hα bubbles (Martin et al. 2002; Sánchez-Cruces et al. 2015). Giant molecular clouds have been detected, but none of them are associated with SSCs A and B (Taylor et al. 1999). The largest CO cloud complex in the galaxy lies to the east of cluster 10 outside our FoV.

Long-slit spectroscopic observations have established the presence of WR stars in SSC-A, whereas no WR stars have been detected in SSC-B (González-Delgado et al. 1997). Using narrow-band *HST* imaging observations with the F469N filter, Buckalew et al. (2000) have inferred the presence of WR features from five SSCs, including SSC-A, and seven individual stars, and nebular emission from three additional point sources. Kobulnicky & Skillman (1997) reported faint He II nebular emission at some of the locations along the long slits they had used. However, no extended He II λ4686 nebular emission has been yet detected in this galaxy. In this paper, we present our results obtained from spectral mapping of the central zone that includes both the SSCs A and B.

In Section 2, we describe the observations and the data reduction. Techniques for separating the He II λ4686 emission lines of stellar origin from nebular origin are also detailed in this section. In Section 3, we present the maps in these two components and compare them with the maps available at the *HST* resolution. Section 4 deals with the calculation of the number of WR stars and the ionizing photon rate of doubly ionized helium. The ionization budget is discussed in Section 5, and our conclusions are given in Section 6. Measured data in individual fibre spectrum are presented in Appendix A.

2 OBSERVATIONS, REDUCTION, AND DATA ANALYSIS

2.1 Observations

Spectroscopic observations of the central part of NGC 1569 (RA=04:30:48.5, DEC=+64:50:55.5) were carried out using the recently available MEGARA instrument at the 10.4 m GTC. MEGARA provides multi-object and integral field spectroscopy at low, medium, and high spectral resolutions $R_{\rm FWHM} \equiv \lambda/\Delta\lambda$ ∼6000, 12 000, and 20 000, respectively, in the visible wavelength interval from 3650 to 9700 Å, through 18 spectral configurations [$\Delta\lambda$=full width at half-maximum (FWHM) of a line]. The IFU, also named Large Compact Bundle (LCB), covers an area on the sky of 12.5 arcsec × 11.3 arcsec with 567 fibres for a spaxel size of 0.62 arcsec. To perform simultaneous sky subtraction, the IFU fibres are supplemented by another 56 fibres distributed in 8 minibundles of 7 fibres, located at the edge of the field at distances from 1.7 to 2.5 arcmin from the centre of the LCB. The complete set of 623 fibres is mounted in the LCB spectrograph pseudo-slit. Additionally, a set of robotic positioners hosts 92 minibundles of 7 fibres each,

also for a spaxel size of 0.62 arcsec, allowing observations in an FoV of 3.5 arcmin × 3.5 arcmin in the multi-object spectrograph mode. These 644 fibres are arranged in a different pseudo-slit interchangeable with the LCB pseudo-slit. For a complete description of MEGARA performance at GTC and the first scientific results obtained during the instrument commissioning, see Carrasco et al. (2018) and Gil de Paz et al. (2018, 2020).

The observations reported here were carried out as part of MEGARA guaranteed time on 2019 February 9 in queue mode under dark sky and photometric conditions. The data were obtained using the IFU mode in combination with the LR-B volume phase holographic grating, centred at 4800 Å, covering the spectral range from ~4330 to 5200 Å for a resolution of FWHM=0.78 Å with a reciprocal dispersion of 0.21 Å per pixel. Three 1200 s exposures were taken at airmasses between 1.25 and 1.30 and a seeing of ~0.9 arcsec. For flux calibration, the spectroscopic standard star HR 5501 was observed in the same set-up as for NGC 1569. Bias, flat-field, and arc lamp images were also obtained as part of the data package.

2.2 Primary data reduction

The primary reduction of the data set was carried out using the standard MEGARA data reduction pipeline (DRP; Pascual et al. 2018). As described above, the MEGARA/IFU data consist of 623 spectra corresponding to 567 objects and 56 sky fibres, arranged into groups of multiple minibundles. In the spectral image, these groups are separated by gaps and have progressively smaller number of minibundles as they were built to reconstruct the curvature of the pseudo-slit at the focal plane of the MEGARA spectrograph. Flat-field images are used to trace the locus of each of the 623 spectra using an automatic routine. The routine fits simultaneously 623 Gaussians every 200 columns and then interpolates the parameters of the Gaussian for each spectral pixel. With this information, the routine generates a weight map for every fibre that is applied to the data in order to perform the extraction. The procedure allows correcting the flux of each fibre for cross-talk contamination from adjacent fibres to a level of a few per cent, depending on the quality of the spectrograph focus during the observation and the shape of the spectral point spread function (PSF) for each wavelength and fibre.

A shift along the pseudo-slit axis of the trace locus with dome temperature has been noticed, which needs a correction of the locus for each observed frame. We used sky lines to measure interactively the shifts, which are found to be ~2 pixels for the three spectral images used in this work. The final product of the DRP is a wavelength-calibrated, sky-subtracted 2D spectral image. This image contains 623 spectra, one spectrum corresponding to each fibre. The standard star is also reduced in an identical fashion. Spectra of all fibres containing the standard star are summed to extract a 1D spectrum, which is used to obtain the flux sensitivity curve using the IRAF[1] routines for this purpose. The resulting sensitivity curve is used to obtain the flux-calibrated 2D images in selected spectral lines and the 3D data cube.

In Fig. 1, we show spectra of four fibres illustrating the detection of broad (top two panels) and narrow (bottom two panels) He II λ4686 features. The Balmer lines H β and H γ, and the [O III] λ5007 Å line are also indicated.
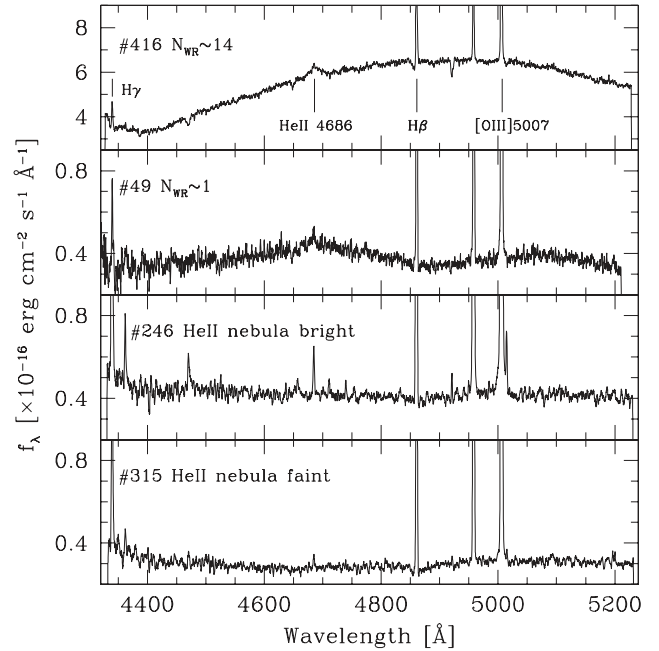
Figure 1. Spectra of individual fibres selected to illustrate broad emission at He II λ4686 corresponding to WR stars (top two panels) and narrow He II λ4686 from ionized nebula (bottom two panels). Four emission features are marked in the topmost spectrum. Fibre#416, which belongs to SSC-A, illustrates the case of a spectrum containing multiple WR stars, whereas fibre#49 illustrates the spectrum of a marginal detection of a WR star. Fibres#246 and #315 are examples of zones with bright and faint nebular He II λ4686 lines, respectively.

2.3 Line maps, data cube, and astrometry

The positions of the fibres in the image plane with respect to the image centre are given in millimetres in the image headers. The 2D spectral image is converted into a 3D data cube using these fibre coordinates. A plate scale of 1.212 arcsec mm^{-1} and a fibre diameter of 0.62 arcsec were used to transform the image coordinates from Cartesian to equatorial systems. To create a map at any sampled wavelength (or a selected band corresponding to a line or a continuum region), we deposited the flux at that wavelength into hexagonal areas (the hexagonal spaxel is inscribed in a circle of 0.62 arcsec diameter), which correctly simulates the FoV of each fibre on the sky. Alternatively, to visualize extended emission, we also created smooth images by depositing the flux of a fibre into a highly oversampled pixel (size=0.021 arcsec) and then convolving it with Gaussian kernel of σ=half the fibre size (0.31 arcsec). Finally, the World Coordinate System header parameters were updated to force the RA and DEC of SSC-A to their values (RA=04:30:48.233, DEC=+64:50:58.59) in the *Gaia*-DR2 system. After creating the image, we measured a mean coordinate error of ~0.3 arcsec for different sources in the resulting image.

We used the QFitsView facility (Ott 2012) for a quick visualization of the data cube and inspection of spectral features associated with known structures in the image. However, all analyses were carried out on the spectrum of an individual fibre or a sum of spectra of neighbouring fibres associated with a physical source. A data cube from the 2D spectral data was constructed using MEGARARSS2CUBE,[2]

---

[1]IRAF is distributed by the National Optical Astronomy Observatories, which are operated by the Association of Universities for Research in Astronomy, Inc., under cooperative agreement with the National Science Foundation.

[2]MEGARARSS2CUBE is a tool written in PYTHON to convert MEGARA reduced data products from the RSS format obtained with megaradrp to a more user-

whereas the generation of line maps and their astrometry, extraction of spectra for physical regions, and measurement of line fluxes were all carried out using our own scripts[3] in the IRAF environment.

We calculated the error as the 1σ deviation, σ_l, on each measured line flux using the expression (Tresse et al. 1999)

$$\sigma_l = \sigma_c D \sqrt{\left(2N_{pix} + \frac{EW}{D}\right)}, \tag{1}$$

where D is the spectral dispersion in Å per pixel, σ_c is the mean standard deviation per pixel of the continuum, N_{pix} is the number of pixels covered by the line, and EW is the equivalent width of the measured line. We used the value of FWHM to substitute for N_{pix}.

2.4 Ancillary data

We used *HST* images in the F555W (ACS/HRC), F814W (ACS/WFC), F658N (ACS/WFC), and F469N (WFPC2) bands to associate our spectra to known structures in the image. All the *HST* images were brought to *Gaia*-DR2 coordinate system using the *Gaia* stars in the *HST* images. The first two images allow us to locate the stars and clusters, whereas the latter two trace the Hα and He II λ4686-emitting sources, respectively. We used the identifications of the SSCs by Hunter et al. (2000) and WR and nebular He II sources by Buckalew et al. (2000). We also used the *Chandra*/ACIS X-ray image in the 0.2–10 keV band from Sánchez-Cruces et al. (2015) in order to locate the point and diffuse X-ray sources with respect to the optical sources.

3 DETECTION OF WR AND NEBULAR HE II λ4686 EMISSION

A simple visual inspection of the 2D spectral image suggested the presence of a feature around 4686 Å in many fibre spectra. Gaussian profile fitting of this feature suggested that in most cases the feature is narrow with FWHM$\sim$1–2 Å, comparable or slightly above the resolution of the spectrograph. In some other fibres, the feature is broad with FWHM>6 Å. These narrow and broad components are illustrated in the bottom two and top two spectra in Fig. 1, respectively. The narrow feature is easily identified as the He II λ4686 emission line from the ionized nebula, whereas the broad component is identified as the blue bump (BB), which is the distinguishing characteristic of WR stars. The BB is a broad spectral feature between 4600 and 4700 Å, and consists of broad lines of He and/or N ions from nitrogen-rich WR stars (WN-types), or He and/or C ions from carbon-rich WR stars (WC-types). Among these, the prominent N and C lines are N III $\lambda\lambda$4634/41, N V $\lambda\lambda$4603/20, C III $\lambda\lambda$4647/66, and C IV λ4658. WC stars, and hence lines from C ions are generally absent in low-metallicity environments (see e.g. fig. 8 in López-Sánchez & Esteban 2010). Additionally, the nebular lines He I λ4713, He II λ4686, and [Fe III] λ4658 can also contribute to the BB. Some spectra showed both narrow and broad He II λ4686 features, which required an analysis using multi-Gaussian fitting for the recovery of each component.

Another factor that affects the measurement of fluxes of relatively faint lines is determining the precise shape of the continuum, which requires a signal-to-noise ratio (SNR) of at least 10 in the continuum

on either side within $\sim$100 Å of the line of interest. In most continuum-weak fibres, this condition is not met. For example, the SNR of the continuum in the bottom three spectra in Fig. 1 is $\sim$5 at 4400 Å and $\sim$9 at 4800 Å. On the other hand, the top spectrum, which belongs to SSC-A, has a minimum SNR of 23 at 4400 Å, increasing to 43 at 4800 Å. Stellar absorption lines, most of which are reported by González-Delgado et al. (1997) for SSC-A, can be seen in the topmost spectrum.

3.1 Multicomponent Gaussian decomposition of the BB

It is well established that the individual lines that contribute to the BB can be extracted from multicomponent Gaussian decomposition technique (see e.g. Brinchmann, Kunth & Durret 2008). We hence carried out multi-Gaussian decomposition fittings using a custom-made code that uses the IDL routine LMFIT[4] (see Gómez-González et al. 2020). Before fitting multiple Gaussians, a continuum level is defined for each spectrum in a two-step procedure. First, a large-scale continuum is defined for each spectrum using the task *continuum* in IRAF, by fitting a high-order polynomial (spline3, order=11) passing through carefully chosen line-free bins in the entire wavelength range of the observed spectrum. Secondly, any residual local continuum around the BB is accounted for by linearly interpolating line-free zones on either side of the BB. Two of the three parameters, the peak intensity I_0 and the line width σ that define each Gaussian, were left free. Any line with an FWHM>6 Å is defined as a broad line associated with a WR star. The third parameter, λ_0, is assigned to the rest wavelength of one of the expected lines from WR stars. The fitting program is executed interactively, where the bright nebular lines are fitted first, followed by the He II broad component. Residuals are examined for a peak near any of the expected line wavelengths. If present, a second broad line is fitted and residuals are re-examined. While fitting this second line, the σ and I_0 of the first line were left free. The process continues examining the residuals and adding a new line until the residual flux is less than 3 times the root-mean-square (RMS) noise of the spectrum. In the iterative process, any faint nebular lines are fitted, if needed. The method is able to recover the He II λ4686 components from WR (broad) and nebula (narrow) even when both are present in a single spectrum. Fig. 2 illustrates the multi-Gaussian fits for spectra from three individual fibres that require both broad and narrow He II λ4686 lines (left), only a broad line (middle), and only the narrow line (right). None of our fibre spectra showed broad lines from nitrogen or carbon ions. A feature is recovered in many fibres at $\lambda = 4658$ Å (see the spectra in the middle and right-hand panels), which matches the wavelength of the C IV λ4658 (broad) feature. However, the width of this line is comparable to that of nebular lines, and hence we identify this feature with the nebular (narrow) line [Fe III] λ4658.

We used the fitting program to automatically identify broad and narrow He II λ4686 features in each of the 567 spectra. As mentioned above, the flux at the peak of the fitted Gaussian should be at least 3 times the noise level for it to be considered a detection. The narrow component, which is of nebular origin, is detected in 262 of these fibres and the broad component in 50. 25 of the spectra showing a broad component have an associated narrow component, whereas the remaining 25 show only a broad component.

---

[3]MEGARA-related IRAF scripts are available on request to the first author.

friendly 3D data cube, available as a repository in GitHub: https://github.com/javierzaragoza/megararss2cube.

[4]The LMFIT function (lmfit.pro) does a non-linear least-squares fit to a function with an arbitrary number of parameters. It uses the Levenberg–Marquardt algorithm, incorporated in the routine *mrqmin* of Numerical Recipes in C (Press et al. 1992).
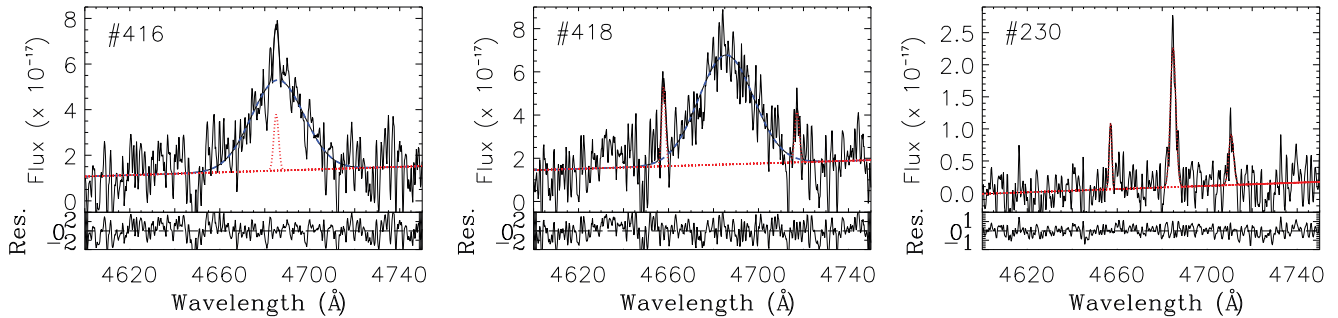
Figure 2. Multi-Gaussian fits to the BBs of individual fibres: broad He II λ4686 line (blue) and narrow He II λ4686 nebular line (red) are shown for three representative fibre spectra that require: both the broad and narrow components (left; fibre#416), only the broad component (middle; fibre#418), and only the narrow component (right; fibre#230). The fitted continuum is shown by the red straight line, and the residuals of the fit are shown below each fit. The fluxes in the fitted spectra as well as in the residual are in units of $10^{-17}\,\mathrm{erg\,cm^{-2}\,s^{-1}\,\AA^{-1}}$. The middle and right spectra show additional narrow lines that we attribute to the [Fe III] λ4658 and He I 4713 nebular lines.

3.2 Location of fibres with WR features

In Fig. 3, we show the positions of all the 50 individual fibres with broad He II λ4686 detections (hexagons),[5] overlaid on an RGB colour-composite image formed by *HST* images in the F814W, F555W, and F469N filters, shown as red, green, and blue colours, respectively. This set of images was chosen in order to highlight the candidate WR stars, which are expected to be continuum-bright sources with He II λ4686 excess. The red and green images having been taken using broad-bands trace continuum sources, whereas the blue image traces sources that have contribution from emission lines in the 4650–4720 Å range. The He II λ4686 line is the most likely contributor to this image, but as the spectra in Fig. 2 illustrate, the nebular lines [Fe III] λ4658 and He I λ4713 could also contribute in this filter. Thus, bluish-looking continuum-bright sources in this image are the likely WR candidates. Buckalew et al. (2000) used the F469N image in combination with continuum and nebular images to identify WR candidate sources. They classified these as cluster, stellar, and unknown origin sources, and named them as C1 to C4, S1 to S6, and U1 to U3 sources, respectively, which are all identified in the figure. In addition, we identified stellar clusters catalogued by Hunter et al. (2000) (numbers 15, 28, 29, and 30) and the two well-known SSCs A and B in the figure. Cluster C4, which lies just outside our FoV and is identified as cluster 10 by Hunter et al. (2000), is the ionizing cluster of the brightest H II region in this galaxy.

The presence of the He II λ4686 broad component is the characteristic signature of a WR star. However, given that our observations were carried out at ∼0.9 arcsec seeing and the fibres cover a diameter of 0.62 arcsec, several adjacent fibre spectra should also show up the broad feature in order to associate the inferred feature with the detection of a WR star. Out of the 50 fibres where we inferred He II λ4686 broad component, 18 contiguous fibres are associated with SSC-A. Some of these fibres could be associated with candidate stellar sources S3, S4, and S5, which are located within the seeing-convolved image of SSC-A.

Of the remaining detections, we infer two locations with four (#417, 419, 421, and 423; on the top-left) and three (#145, 149, and 153; on the top-middle) contiguous fibres, associated with them. However, a careful scrutiny of the fibres associated with these locations revealed that these fibres are physically next to one of the 18 fibres belonging to SSC-A on the pseudo-slit, and hence the detected broad bump is likely arising due to residual cross-talk from SSC-A.

Hence, we ignore the detections in these seven fibres. The rest of the inferred He II λ4686 broad component corresponds to 25 single-fibre detections, scattered all over the image. One of these detections (#413) is due to cross-talk with SSC-A. Of the remaining detections, two coincide with the previously reported candidate stellar sources S2 and S6. If these single-fibre detections come from real sources, spectra extracted by summing spectra of fibres adjacent to the location of these fibres should also show a broad He II λ4686 feature. We carried out the Gaussian decomposition of the BB with the specific purpose of detecting these broad features in spectra obtained by summing spectra of at least three fibres around the one where we detected the broad feature. None of these summed spectra around the 25 single-fibre detections showed a broad component. Uncertainty in defining the continuum is the likely reason for the feature to vanish in summed spectra in spite of them being detected; i.e. the peak flux of the fitted broad (FWHM > 6 Å) Gaussian profile is > 3 times the RMS error of the continuum, in individual fibre spectra. The spectrum for fibre #49 in Fig. 1 is one such example. Deeper observations would be required to ascertain the nature of these sources. We consider these detections as marginal and in Section 4.3 we compare their fluxes to that expected from typical WNL-type WR stars.

The summed spectra allow us to understand the reasons why Buckalew et al. (2000) interpreted the observed excess emission in the *HST*/F469N band in C3, S2, and S6 as originating in WR stars. It may be recalled that imaging observations cannot distinguish between the narrow and broad components. Buckalew et al. (2000) assumed it to be a WR detection, if the position of a star or cluster coincides with the position where an excess flux is detected in the F469N band. This selection criterion does not contemplate the presence of extended He II λ4686 nebular emission. As we discuss in detail below, we have detected extended He II λ4686 nebular emission in the central zone of NGC 1569. Objects C3, S2, and S6 are stellar sources in which we detect narrow nebular He II λ4686 and [Fe III] λ4658 lines in our spectra (see the bottom three spectra in Fig. 4). The narrow lines are not originating in the stellar sources, and are instead part of the extended nebular emission. At the location of the three sources of unknown origin (U1, U2, and U3), we detect only narrow He II λ4686 line; these sources are also part of the extended nebula.

Our spectral data are used to infer the WR population in known clusters in our FoV. Apart from SSC-A, where we already demonstrated the presence of WR stars, our FoV includes clusters SSC-B, 28, 29, and C3. Among these, previous spectroscopic observations have already ruled out the presence of WR features in SSC-B (e.g.

[5]See Fig. A1 in the appendix for the identification numbers of each fibre.
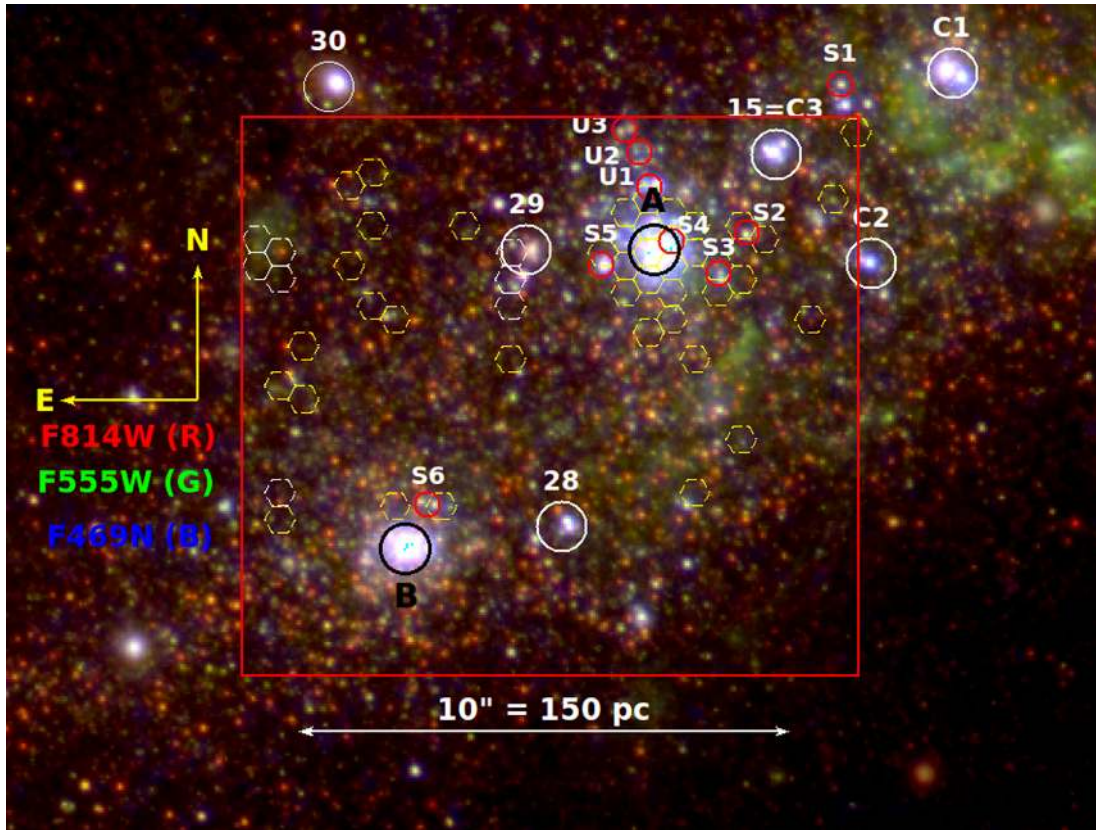
Figure 3. A colour-composite RGB image of the central starburst zone of NGC 1569. The image is formed by combining *HST* F814W-, F555W-, and F469N-band images, as red, green, and blue components, respectively. MEGARA/IFU FoV (12.5 arcsec × 11.3 arcsec; red rectangle) and image orientation (compass) are shown. The locations of the fibres where we detected a broad He II λ4686 component are shown by hexagons. The prominent objects in the FoV are identified. These include the two massive clusters SSC-A and SSC-B, and four other clusters (15, 28, 29, and 30) from Hunter et al. (2000). WR sources identified by Buckalew et al. (2000) using the displayed *HST* F469N image, which intercepts the He II λ4686 line, are shown. These include four clusters with WR stars (C1, C2, C3, and C4) and six WR stars (S1, S2, S3, S4, S5, and S6). Three sources (U1, U2, and U3) classified as of unknown origin by Buckalew et al. (2000) are also shown. The He II λ4686 broad feature is detected in 18 adjacent fibres associated with SSC-A. The circles enclosing cluster candidates have a diameter of 1 arcsec, and hexagons have an equivalent diameter of 0.62 arcsec.

González-Delgado et al. 1997). No WR stars were inferred in F469N images by Buckalew et al. (2000) from sources 28 and 29, whereas C3 is a candidate WR cluster. We extracted spectra around all these sources, as well as for SSC-A (C4), by adding spectra of seven fibres around the location of these clusters. Unfortunately, cluster 29 spectrum suffers from cross-talk problem as several of its fibres are adjacent to some of the fibres of SSC-A on the pseudo-slit. We hence did not carry out an analysis of search for WR stars in this cluster. Multi-Gaussian analysis was carried out on these summed spectra, which are shown in Fig. 4. These fits establish the presence of WR features in summed spectra of SSC-A, and their absence in SSC-B, 28, and C3. The figure also shows (last two panels) the results of the fits to the summed spectra for S2 and S6. Given the closeness of these sources to SSC-A and SSC-B, respectively, we summed spectra of only three adjacent fibres in these cases. The broad He II λ4686 component is not recovered in these summed spectra.

3.3 He II λ4686 nebular morphology

We now discuss the results obtained by multi-Gaussian fitting to recover the He II λ4686 nebular line. Unlike the broad component, the narrow He II λ4686 line, which is of nebular origin, is detected in nearly half of the total fibres. The fibre fluxes and locations are used

to create a map, which is shown in Fig. 5 as the green component of the RGB image. The *HST* images in the F658N (H α + continuum) and F555W bands are used for the red and blue components, respectively. These latter images help us to see the large-scale distribution of ionized gas and stars at the *HST* resolution. Contours corresponding to He II λ4686 nebular line surface brightness of 3, 12, and 20 × 10⁻¹⁷ erg cm⁻² s⁻¹ arcsec⁻² are shown.

Clearly, the He II λ4686 narrow emission is not confined to a few point sources, but instead is part of an extended nebula. This emission is distributed along a semicircular arc of 150 pc (10 arcsec) diameter. The brightest part of the He II λ4686 nebula lies to the south-west of SSC-A at a distance of ∼40 pc (2.5 arcsec). This brightest part is also the zone closest to SSC-A, where there is an increase in the H α surface brightness, and corresponds to the H II region numbered 3 by Waller (1991). The nebular arc is widest near this zone, reaching ∼40 pc width. The centre of the semicircular arc does not coincide with SSC-A, and instead is shifted to the east of it by ∼40 pc, roughly coincident with cluster 29. Unfortunately, our FoV does not cover the northern part; hence, we cannot conclude whether the observed arc is part of a complete circular nebula or not. There is no evidence for arc-like structure in the H α image on the northern side, nor any of the ionized superbubbles (sb) identified by Sánchez-Cruces et al. (2015) match our He II λ4686-emitting segment or its possible northern counterpart. This can be due to the lower sensitivity of
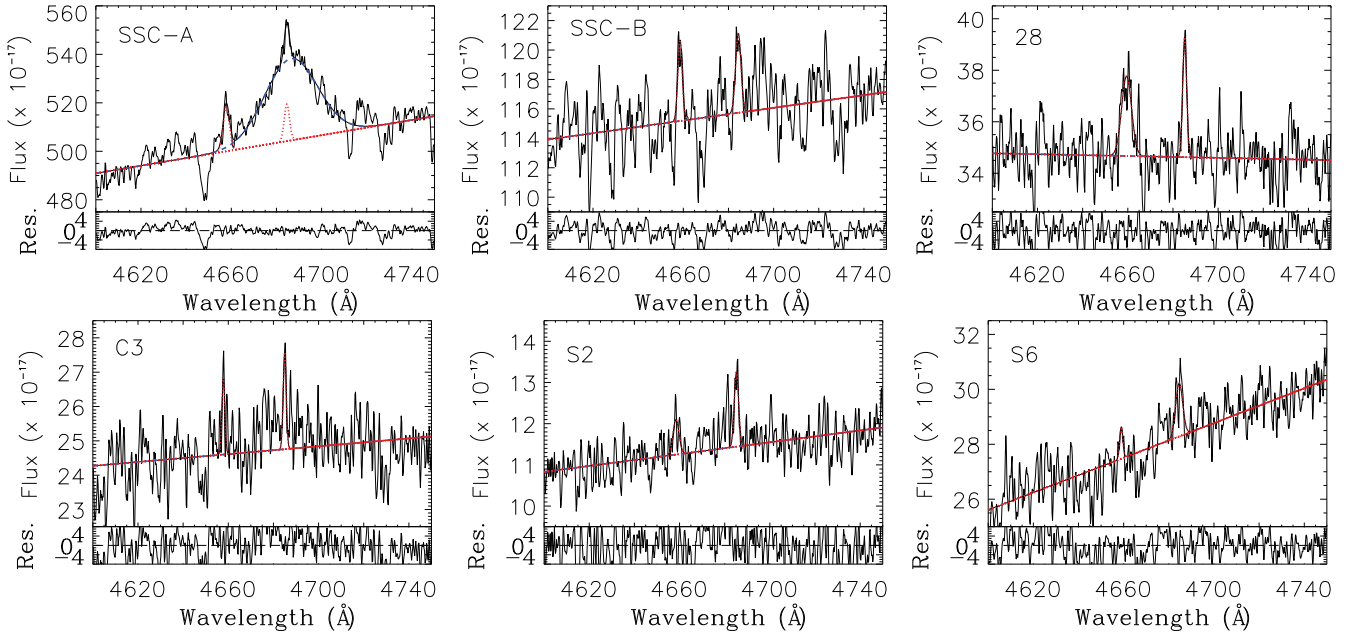
Figure 4. Multifibre summed spectra around the BB of SSC-A and other cluster and stellar sources in the FoV of MEGARA/IFU. No WR stars are detected in clusters SSC-B and 28. Star cluster C3 and stellar sources S2 and S6, where the presence of WR stars has been previously reported from the analysis of the *HST* F469N-band narrow-band images, only show nebular lines in our spectra. The fluxes are plotted in units of 10^{-17} erg cm^{-2} s^{-1} Å^{-1}, and the bottom panel of each plot shows the residual flux in the same units.
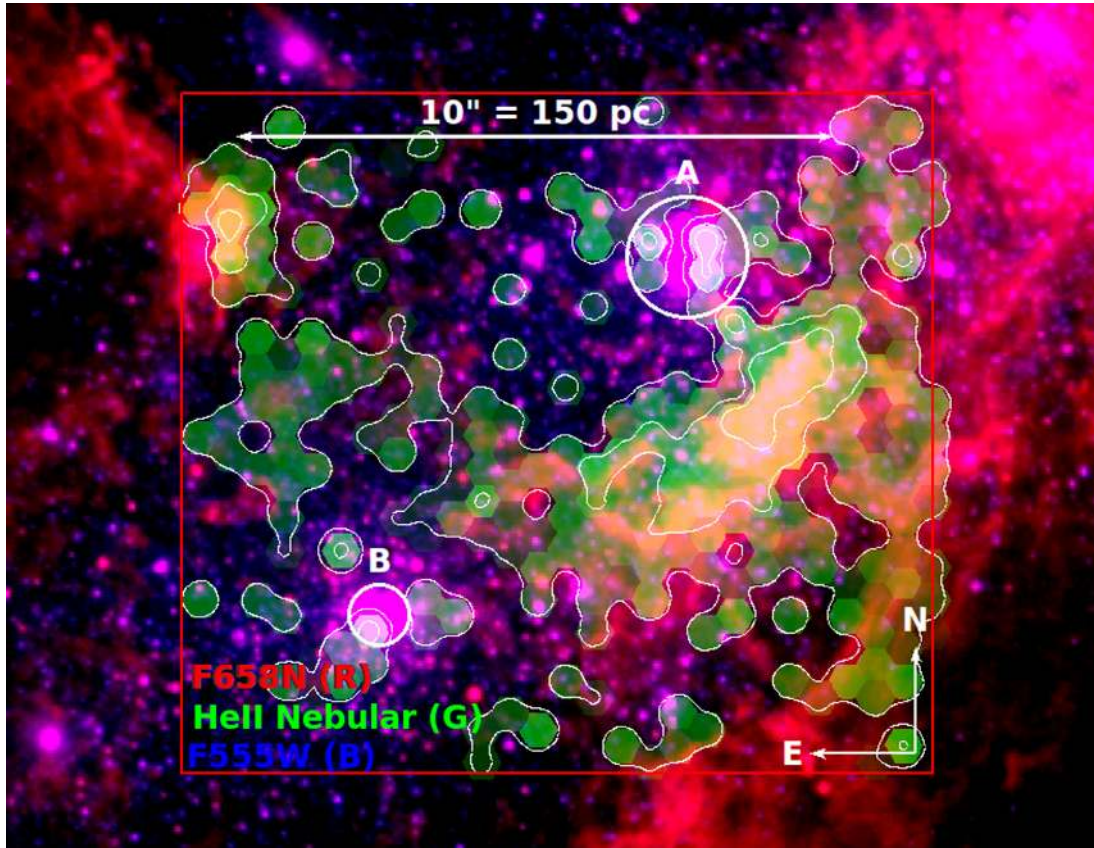
Figure 5. Colour-composite RGB image showing the morphology of the He II λ4686 nebular emission (white contours englobing green hexagons) with respect to that of the Hα emission (*HST* F658N band shown in red) and stellar continuum (*HST* F555W image shown in blue). Clusters A and B are marked. The contours correspond to surface brightness levels of 3, 12, and 20 × 10^{-17} erg cm^{-2} s^{-1} arcsec^{-2} in the He II λ4686 nebular line. The nebular emission is weak from SSCs A and B, and is distributed along a semicircular arc with the most intense emission coming from a zone ∼40 pc south-west of SSC-A.

Fabry–Pèrot images presented by Sánchez-Cruces et al. (2015) in comparison to the *HST* images. The He II λ4686-emitting segment lies between the superbubbles classified as sb4, sb5, sb6, and sb7. The He II λ4686 nebular emission is weak in the immediate vicinity of SSC-A and SSC-B.

By mapping the He II λ4686 nebular emission, we can obtain the total flux in this line, and from this, the ionization requirements. The data need to be corrected for extinction from dust along the line of sight in the Galaxy as well as the dust in NGC 1569, before we can carry out these calculations. The availability of the extinction-sensitive Balmer lines H β and H γ in our data set allows us to obtain the extinction from each fibre spectrum. We describe the procedure adopted for extinction correction in the next section.

4 EXTINCTION-CORRECTED NUMBER OF WR STARS AND THE HE II IONIZING PHOTON RATE

In this section, we present the extinction map of the zone covered by our IFU observations, and obtain the He II λ4686 luminosity of the broad and narrow lines, corrected for extinction. The luminosity in the broad component is used to calculate the number of WR stars inferred from our observations, whereas the luminosity in the narrow component is used to obtain the He$^+$ ionizing photon rate. We used the emission-line intensities of Balmer lines (H β and H γ) in our IFU spectra to create maps of the ionized nebula and extinction. We note that the stellar continuum of unresolved populations, in general, experiences lesser amount of attenuation as compared to that experienced by the ionized gas (Calzetti, Kinney & Storchi-Bergmann 1994; Mayya & Prabhu 1996). Hence, the number of WR stars derived after correcting the broad component luminosity for nebular extinction could be an overestimate.

4.1 Extinction map of the observed zone

In Section 3.1, we described the procedure we followed for decomposing the narrow and broad components of the He II λ4686 feature. We measured the fluxes and related quantities of the H β and H γ nebular lines in each fibre spectrum using the single-Gaussian fitting option of the IRAF task *splot* in batch mode. The line fluxes in each fibre are then transformed into maps using the procedure described in Section 2.3.

H β and H γ emission fluxes were used to obtain the extinction from each fibre spectrum, where both of these lines were detected, using the Balmer decrement method for case B recombination of a typical photoionized nebula ($T_e = 10\,000$ K, $n_e = 100$ cm^{-3}; Osterbrock & Ferland 2006) and the reddening curve of Cardelli, Clayton & Mathis (1989). Only spectra with an SNR of at least 3 in both the lines are used. The H β line is detected at SNR>7 in all the 567 fibres. This line is well resolved with the FWHM of the fitted Gaussian varying between 1 and 2 Å. Some spectra clearly showed signs of more than one velocity component. In 86 per cent of these spectra (487), the H γ line is also detected at SNR≥3, enabling A_V measurements in all these spectra. The resulting values along with the errors are given in the last two columns of Table A1. However, all measurements are not reliable. A source of error in the derived A_V is the uncertain correction of the underlying absorption in the H β and H γ lines. We used a uniform 1 Å of correction in EW proposed by González-Delgado et al. (1997) for both the H β and H γ lines. The underlying absorption affects spectra at locations where we detected strong continuum, some of which belong to the
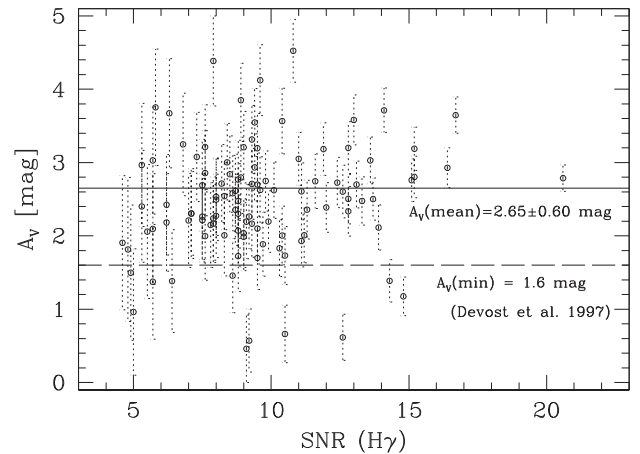

Figure 6. Visual extinction A_V obtained from the H β and H γ nebular lines is plotted against the SNR of the H γ line, which is the weaker of the two lines. Only 106 spectra for which the EW(H γ)>8 Å are considered for plotting. Among the plotted points, 90 per cent lie above the dashed horizontal line, which corresponds to the minimum A_V in the entire galaxy found by Devost, Roy & Drissen (1997). The mean value of our measurements is shown by the solid horizontal line. See Section 4.1 for further details.

WR stars. Thus, it is reasonable to use the A_V obtained for continuum-weak, or alternatively high-EW, spectra for carrying out fibre-to-fibre A_V corrections. As H γ is the more critical of the two lines in A_V measurements, we used only those spectra that have EW(H γ)>8 Å. This left us with the best 106 measurements of A_V. The resulting A_V values are plotted against the SNR of the H γ line, which is the fainter of the two lines used for determining extinction, in Fig. 6. The estimated error on each measurement is shown, which is typically ∼0.5 mag. These error bars do not take into account errors introduced by the uncertain correction for the underlying stellar absorption; e.g. the A_V values would be ∼0.2 mag higher or lower depending on no correction or correction of 2 Å (instead of the assumed 1 Å), respectively.

Devost et al. (1997) obtained A_V using the H α and H β lines for 16 zones spread over the entire galaxy. They found that all the zones have $A_V \geq 1.6$ mag, with the minimum value corresponding to a zone in an ionized bubble, which is outside our FoV. They proposed that this minimum value corresponds to the extinction from the Galactic dust along the line of sight to NGC 1569. Grocholski et al. (2012) obtained a marginally higher value ($A_V = 1.8$ mag) using an analysis of the RGB of the resolved stellar population in the outer disc of the galaxy. There are many independent measurements of the Galactic extinction in the direction of NGC 1569. Using the line-of-sight H I observations, Burstein & Heiles (1984) and Schlegel, Finkbeiner & Davis (1998) obtained values of $A_B = 2.03$ mag (equivalent to $A_V = 1.55$ mag) and $A_V = 2.3$ mag, respectively. Israel (1988) and Origlia et al. (2001) analysed the UV spectra of NGC 1569 and suggested a foreground extinction of $A_V = 1.7$ mag. More recently, Schlafly & Finkbeiner (2011) obtained a value of $A_V = 1.9$ mag based on the colour excess of SDSS stars that have spectroscopic data.

All these values, with the exception of one (Schlegel et al. 1998), are compatible with a Galactic extinction value of $A_V = 1.6$ mag proposed by Devost et al. (1997) after taking into account measurement errors. We show this lower limit by a dashed line in Fig. 6. 90 per cent of our measurements are above this line. 9 of the 11 measurements below this line are consistent with $A_V = 1.6$ mag if we calculate A_V without any absorption correction. Thus, taking into
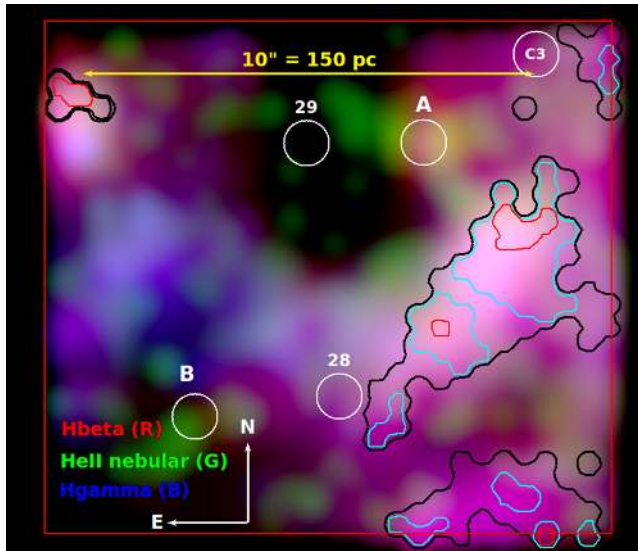
Figure 7. Extinction contours superposed on the MEGARA RGB nebular images. Smoothed images in Hβ, He II λ4686, and Hγ are used as red, green, and blue components, respectively. The contours corresponding to $A_V = 1.6$, 2.6, and 3.6 mag are shown in black, cyan, and red colours, respectively. The noise in the measured fluxes in individual fibre spectra did not allow the determination of reliable A_V values outside the black contours, though emission is seen in this smoothed image. Known sources in the FoV are labelled. The zone with the highest He II λ4686 nebular emission (south-west of SSC-A) is also the zone with the highest A_V. The nebular emission follows a semicircular arc of ~150 pc diameter.

account external errors, our data are in agreement with a minimum $A_V = 1.6$ mag proposed by Devost et al. (1997). The rest of the H II regions observed by Devost et al. (1997) have a mean value of $A_V = 2.26$ mag, implying an average internal extinction of 0.66 mag for NGC 1569. We obtain a mean $A_V = 2.65 \pm 0.60$ mag for 95 spectra having $A_V > 1.6$ mag. This implies an average internal extinction of 1.05 mag for the zone covered by our observations.

We used the A_V values obtained in these 95 fibres to create an extinction map, whose contours are shown in Fig. 7, overlaid on a nebular colour-composite image, formed by combining Hβ, He II λ4686, and Hγ images as red, green, and blue components, respectively. All the three nebular images are smoothed using a Gaussian kernel of 0.31 arcsec following the procedure described in Section 2.3. As the Hγ-to-Hβ ratio is sensitive to extinction, the colour in the image is expected to change from blue to red as extinction increases. The zone with the highest He II λ4686 nebular surface brightness (south-west of SSC-A) is also the zone with the highest A_V, reaching values of ~4 mag. Extinction smoothly decreases from this point towards the south-east, reaching the Galactic values of $A_V = 1.6$ mag at the boundaries of the detected zone. High extinction is also inferred from the zone with weak nebular emission in the bottom-right corner of the image, and a zone at the top-left corner of the image. Nebular lines are weak in almost all continuum-bright regions, including in SSC-A, which prevented us from determining A_V for these sources. We have assigned the Galactic values of $A_V = 1.6$ mag to all regions outside the black contours, where A_V could not be reliably measured. Fig. 7 also allows us to compare the large-scale morphology of He II λ4686 nebula (green) with that of the ionized gas traced by Balmer lines at the same resolution. The H II gas is also distributed along the semicircular arc traced by the He II nebula, both showing a clear hole in the central zone of their intensity distributions.

4.2 Total He II ionizing photon rate

The availability of an extinction map allows us to apply fibre-to-fibre extinction corrections. We used a uniform value of $A_V = 1.6$ mag to all spectra where A_V could not be measured reliably. Summing all these fluxes, we obtain a total He II λ4686 flux of 9.13×10^{-14} erg cm^{-2} s^{-1}. This corresponds to an L(He II λ4686) of 1.0×10^{38} erg s^{-1} and a Q(He$^+$) of 1.0×10^{50} photon s^{-1} using the basic photoionization equation from Osterbrock & Ferland (2006),

$$\frac{Q(\text{He}^+)}{\text{photon s}^{-1}} = \frac{L(\text{He II}\lambda4686)}{E_{\lambda4686}} \times \frac{\alpha_B(\text{He}^+)}{\alpha_{\text{eff}}(\text{He II}\lambda4686)} \qquad (2)$$

$$= 1.02 \times 10^{48} \frac{L(\text{He II}\lambda4686)}{10^{36} \text{ erg s}^{-1}}, \qquad (3)$$

where $E_{\lambda4686}$ is the energy of the He II λ4686 photon, and α_B and α_{eff} are case-B recombination coefficients. We used the α_B and α_{eff} assuming reasonable $T_e = 10\,000$ K and $n_e = 100$ cm^{-3} for the nebula. The calculated Q(He$^+$) would change by less than 10 per cent for the entire range of T_e and n_e covered by the photoionized nebulae (Kehrig et al. 2015).

The total extinction-corrected Hβ flux from the same regions is 4.44×10^{-12} erg cm^{-2} s^{-1}. This is equivalent to a Lyman continuum rate Q(H^0) of 1.0×10^{52} photon s^{-1}, using an equation similar to equation (2) but for Q(H^0), which is

$$\frac{Q(\text{H}^0)}{\text{photon s}^{-1}} = 2.10 \times 10^{48} \frac{L(\text{H}\beta)}{10^{36} \text{ erg s}^{-1}}, \qquad (4)$$

where L(Hβ) is the luminosity of the Hβ line. The above equations result in the ratio

$$Q(\text{He}^+)/Q(\text{H}^0) = 0.486 \times \frac{L(\text{He II}\lambda4686)}{L(\text{H}\beta)}. \qquad (5)$$

The luminosity of He II λ4686 corresponds to 2.05 per cent of the Hβ luminosity, which results in a value of Q(He$^+$)/Q(H^0) = 0.0100 ± 0.0002.

The emission EW of Hβ of a starburst population is a well-known age indicator. For unresolved regions, it is one of the quantities easiest to obtain from spectroscopic data. Furthermore, it is independent of extinction as long as the ionizing cluster and the nebula are spatially coincident or there is no differential extinction between cluster stars and nebula. However, in a resolved nebula such as the one discussed here, determination of EW(Hβ) is non-trivial. As the ionized nebula is spatially separated from the ionizing cluster, we made the assumption that the photoionization from SSC-A is responsible for the total observed Hβ flux. With this assumption, we divided the observed integrated Hβ flux by the continuum flux in the integrated spectrum of SSC-A (displayed in Fig. 4), measured close to the Hβ line. We obtained EW(Hβ) under three assumptions. The first one is that the ratio is independent of extinction. In the second case, the continuum flux is corrected by $A_V = 2.3$ mag, and the Hβ flux is corrected for the extinction determined by the Balmer decrement method. In the third case, the same Hβ flux correction was used, but the continuum flux was corrected by making use of the minimum extinction of $A_V = 1.6$ mag. The three assumptions give values of 75, 75, 160 Å, respectively.

4.3 The number of WR stars in the mapped zone

While fitting the BB with multi-Gaussians, we have looked for N (N III $\lambda\lambda$4634/41) and C (C III $\lambda\lambda$4647/66 and C IV λ4658) broad lines in addition to the broad He II λ4686 feature. In all spectra, including that of SSC-A, only one broad component was required, which is the

He II λ4686 line. In some spectra, a nebular [Fe III] λ4658 line is seen at the expected broad C IV λ4658 line, where our fitting procedure would have been able to recover a broad feature even in the presence of an overlying narrow line. The absence of any of the C lines points to the absence of WC stars in the observed zone. Previous observations of SSC-A that had covered the red bump (C IV λλ5801/12) part of the spectrum had already indicated the absence of WC stars (González-Delgado et al. 1997), which is not unusual given that its metallicity is lower than solar (López-Sánchez & Esteban 2010). Thus, we conclude that all our detections originated in WN stars. The relative weakness of N III λλ4634/41 suggests these are WNL stars.

We now estimate the number of WR stars in each of the fibres where the broad He II λ4686 feature was detected in single-fibre spectra. As pointed out in Section 3.2, 18 of these fibres belong to SSC-A, and 8 other fibres are in cross-talk with fibres belonging to SSC-A. Single-fibre detections in rest of the fibre spectra are considered tentative, as the detected broad feature could not be recovered by summing spectra of neighbouring fibres. The number was estimated by dividing the observed luminosity in the He II λ4686 broad feature by the typical luminosity of a WNL star that is $\sim 1.22 \times 10^{36}$ erg s^{-1} (López-Sánchez & Esteban 2010) for the metallicity of NGC 1569. This value is ∼30 per cent smaller than the corresponding value at the Solar metallicity (Vacca & Conti 1992). The observed luminosities of the He II λ4686 broad feature in each fibre need to be corrected for extinction. As discussed above, the A_V values derived at the positions of WR stars are highly unreliable, because of low nebular flux and high underlying Balmer absorptions at these locations. Larsen et al. (2011) found the colours of the resolved stellar population of SSC-A to be consistent with $A_V = 2.3$ mag. This suggests that the internal extinction of the cluster stars is 0.35 mag lower than the mean value of the nebula, as expected for an attenuation law like the one proposed by Calzetti et al. (1994). Hence, $A_V = 2.3$ mag seems the most appropriate value to use to correct the fluxes of the He II λ4686 broad feature from SSC-A. We hence calculate the number of WR stars using this optimum value $A_V = 2.3$ mag. We also calculate the minimum and maximum numbers corresponding to $A_V = 1.6$ and 2.65 mag, respectively.

In Fig. 8, we show the estimated number of WR stars in each fibre where the broad He II λ4686 feature is inferred, including those fibres with tentative detections. The solid symbols joined by solid lines indicate the number using the optimum value for SSC-A of $A_V = 2.3$ mag, whereas the other two lines correspond to minimum ($A_V = 1.6$ mag, triangles joined by dotted lines) and mean nebular ($A_V = 2.65$ mag, circles with dotted lines) extinction. Fibres assigned to SSC-A are identified (red shaded area), as well the eight fibres that are affected by cross-talk with SSC-A (black diagonal hatched area). With the optimum value of $A_V = 2.3$ mag, all the fibres associated with SSC-A have the luminosity of at least 1 WNL star, with one of the fibres (#418) containing as many as 19 WNLs. This fibre belongs to the core of SSC-A. In total, we find 124 ± 11 WNL stars in SSC-A by adding the numbers in each one of the 18 fibres, where the quoted error assumes Poissonian statistics. This number agrees with the corresponding number obtained by fitting the multi-Gaussian on the spectra summed over 19 fibres covering the SSC-A. Detected fluxes correspond to 56 ± 7 and 186 ± 13 WNL stars if we adopt $A_V = 1.6$ or 2.65 mag, respectively. The uncertainty in the modelling of the extended wings of the spatial profile of the PSF of the fibres for those SSC-A spaxels where the WR bump is detected might lead to an underestimation of the total number of WR stars in SSC-A that could be of the order of a few per cent. Among the other single-fibre detections, only sources belonging to fibres #49 and #51 have N_{WR} at least one for $A_V \geq 2.3$ mag. Detected fluxes in the rest of the

fibres are less than the flux expected for a WNL star. As discussed in Section 3.2, these detections were considered as tentative due to the non-recovery of the broad component in spectra obtained by summing spectra of neighbouring fibres.

González-Delgado et al. (1997) have estimated the number of WR stars in SSC-A from their long-slit spectroscopic data assuming an $A_V = 1.6$ mag. Using an older distance estimate of 2.2 kpc, and luminosity of a WNL star of $\sim 1.7 \times 10^{36}$ erg s^{-1} from Vacca & Conti (1992), they estimated 24 WNL stars from their spectra, which corresponds to 66 WNL stars for the values used in our work. Our value for $A_V = 1.6$ mag is comparable with this value. On the other hand, the number of WR stars estimated based on the *HST* narrow-band image in the F469N filter by Buckalew et al. (2000) is 51 ± 19 ($A_V = 1.6$ mag, distance = 2.2 kpc) WNL stars, which corresponds to 141 WNLs for the distance and WNL luminosity used in our work. This is 2.5 times higher than our value. As noted earlier (see Fig. 4 for SSC-A), nebular lines are weak for SSC-A, and hence it is unlikely that this discrepancy comes from the contribution of the nebular lines (e.g. He II λ4686, He I λ4713, and [Fe III] λ4658) to the inferred flux in the F469N filter. Residual error in continuum subtraction because of the strong continuum of SSC-A could be the most likely reason for the overestimation of the number of WR stars.

5 THE IONIZATION BUDGET OF HE II

5.1 Ionization by WR stars

The region of NGC 1569 analysed in this work is dominated by the SSCs A and B in continuum light (Arp & Sandage 1985). Prada, Greeve & McKeith (1994) inferred the presence of red supergiants (RSGs) in both the SSCs A and B. SSC-A is made of two components, separated by 0.2 arcsec (3 pc), called A1 and A2 by De Marchi et al. (1997). González-Delgado et al. (1997) found spectral features characteristic of both the WR stars and RSGs in their ground-based long-slit spectra of SSC-A. Origlia et al. (2001) analysed *HST* UV spectra of SSC-A and suggested that the RSGs and WR features originated in A1 and A2 components, respectively, with the age of the latter component not exceeding 5 Myr. Larsen et al. (2011) carried out photometry of the stars in the periphery of the clusters A and B on the *HST* images to obtain turn-off ages in the colour–magnitude diagram (CMD). They found RSGs in the CMD of SSC-B, but not in SSC-A. If the RSGs are restricted to the A1 component as Origlia et al. (2001) suggested, this implies that this component is centrally concentrated and the stars in the periphery are part of A2, the younger of the two subclusters. Based on the absence of RSGs in the CMD, they derived an upper age limit of 4.5 Myr for this component. On the other hand, they obtained an age of 16 Myr for SSC-B. Thus, at present SSC-A is in the WR phase, when a cluster is most efficient in producing He II ionizing photons. We point out that the bright Hα emission seen at the top-right corner of the image presented in Fig. 5 is due to ionization by cluster 10 (Westmoquette et al. 2007), which coincides with WR cluster C1 of Buckalew et al. (2000). We here investigate whether SSC-A alone is capable of producing the observed luminosity of the He II λ4686 nebular line.

The principal sources of He II ionizing photons in young stellar systems are O stars and their evolutionary products, such as WR stars. These stars have extended atmospheres with high mass-loss rates; hence, a calculation of the rate of He II ionizing photons has to take into account the radiation transfer through these atmospheres. In recent years, such spectra are available from the CMFGEN code (Hillier & Miller 1998; Pauldrach, Hoffmann & Lennon 2001;
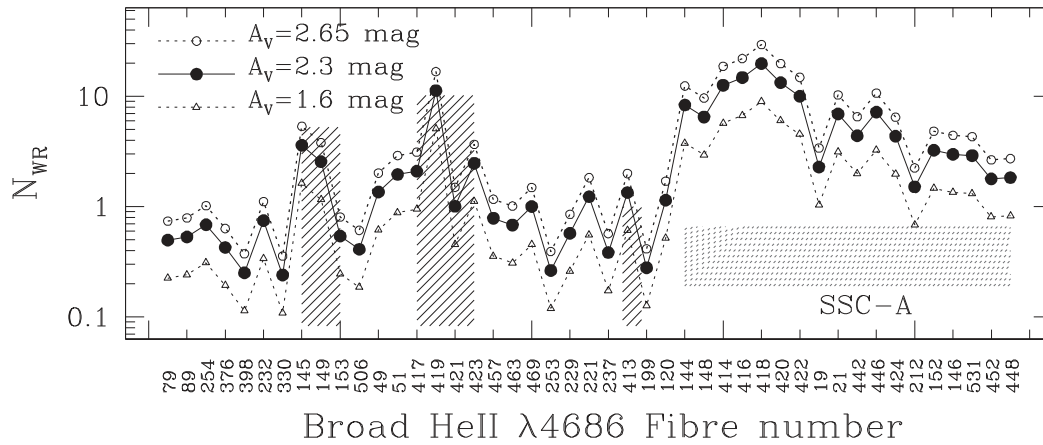
Figure 8. The number of WR stars, defined as the observed He II λ4686 broad-line luminosity divided by the typical luminosity of a WNL star $(1.22 \times 10^{36}$ erg s$^{-1})$, versus fibre number. All 50 individual fibres where we detected broad He II λ4686 feature are shown. The numbers are plotted for three values of extinction: $A_V = 1.6$ mag, the minimum along the line of sight to NGC 1569 (triangles), $A_V = 2.65$ mag, the mean determined for the ionized nebula (open circles), and $A_V = 2.3$ mag, optimum value for SSC-A (solid circles). Fibres belonging to SSC-A, and those that have cross-talk with fibres of SSC-A are indicated by red shaded area, and diagonally hatched area, respectively. SSC-A contains 124 WR stars for $A_V = 2.3$ mag.

Smith, Norris & Crowther 2002) for O and WR stars, and from the Potsdam POWR library (Gräfener et al. 2002) for WR stars. We compared our observed values with publicly available Simple Stellar Population (SSP) models that have incorporated either CMFGEN or POWR spectra in their codes. Calculations are available at discrete values of metallicity. The gas-phase oxygen abundance of NGC 1569 corresponds to $Z = 0.006$ for a depletion of 30 per cent of oxygen on to dust grains and assuming [O/Fe] = 0.0 (Gutkin, Charlot & Bruzual 2016). We illustrate the results for models using $Z = 0.008$, which is the closest metallicity to that of NGC 1569, and comment on the metallicity dependence of the obtained results. A summary of the $Z = 0.008$ models we used is given in Table 1.

The codes we used are STARBURST99 (Leitherer et al. 1999, 2014) with Padova (SB99/Padova; Bressan et al. 1994) and Geneva high-mass-loss (SB99/Geneva; Meynet et al. 1994) evolutionary tracks, PopStar (PopStar/Padova; Mollá et al. 2009) with an updated version of the Bressan et al. (1994) Padova tracks, two versions of GALAXEV: BC03/Padova (Bruzual & Charlot 2003) based on tracks from Bressan et al. (1994) and C&B/Padova (Charlot & Bruzual, in preparation; see Gutkin et al. 2016; Plat et al. 2019) based on tracks from Chen et al. (2015), and the BPASS (Eldridge et al. 2017) that uses Cambridge evolutionary tracks in single (BPASS/single) and binary (BPASS/binary) modes. STARBURST99 and PopStar make use of the CMFGEN code, whereas GALAXEV and BPASS use the POWR code, to model the extended atmospheres of WR stars. We downloaded the latest results from these codes from the websites of the respective codes, uniformly using Kroupa (2001) IMF between 0.15 and 100 M$_\odot$. In the case of BPASS models, the detailed calculations of ratios of different lines, including that of I(He II λ4686)/I(Hβ), have been provided by Xiao, Stanway & Eldridge (2018). We used the ratios corresponding to the ionization parameter of log $U = -1.5$ and an atomic density of 1 atom cm^{-3}. For the rest of the models, we used equation (5) to convert the ratio of He$^+$ to H^0 ionizing photon rates to a flux ratio I(He II λ4686)/I(Hβ).

Results of the comparisons are presented in Fig. 9 on the left-hand panels. Horizontal hatched areas in each panel encompass the entire range of observable quantities with account for observational errors. For I(He II λ4686)/I(Hβ) and Q(H^0), errors are taken as 10 per cent, whereas for the number of WR

stars, the main source of error is the uncertainty in extinction correction.

The model Q(H^0) decreases monotonically with age, whereas the nebular I(He II λ4686)/I(Hβ) ratio has a well-defined peak at $\sim$4 Myr, which corresponds to the appearance of WR stars in the cluster. This ratio is independent of distance, cluster mass, extinction, the chosen nebular parameters (temperature and density), and the choice of IMF parameters, as long as the upper cut-off mass is not very much different from 100 M$_\odot$. Hence, among the three plotted quantities, the age derived from I(He II λ4686)/I(Hβ) ratio is the most reliable. Three models that use Bressan et al. (1994) Padova evolutionary tracks have peak values of I(He II λ4686)/I(Hβ) higher than the observed value in NGC 1569 (see Table 1). The ratio is marginally smaller for model that makes use of the results from the new Padova tracks (Chen et al. 2015), whereas in the other three models this ratio is much lower. All the models reproduce the observationally estimated Q(H^0) for a cluster of mass $(5.5 \pm 0.5) \times 10^5$ M$_\odot$ in its WR phase. The observed EW(Hβ) is also consistent with the value expected during the WR phase for single star evolutionary models (see column 7 in Table 1). The number of WR stars predicted in all models agrees with the best estimation of the observed value to within 30 per cent for the mass inferred above. The WR phase in single star evolutionary models lasts between $\sim$3.5 and 5 Myr. The limits for star cluster age are determined from the condition that the model-predicted number of WR stars for the above inferred mass exceeds the lower limit for the observationally inferred number of WR stars in SSC-A. This age range, as well as the age at which the I(He II λ4686)/I(Hβ) ratio reaches its peak value, is given in Table 1, in columns 5 and 3, respectively.

It is interesting to note that the SB99/Padova and SB99/Geneva models use the same atmospheric models in the WR phase, but Geneva evolutionary tracks have lower I(He II λ4686)/I(Hβ) in spite of having $\sim$25 per cent more number of WR stars. This implies that the low values of I(He II λ4686)/I(Hβ) in the SB99/Geneva models are not due to lack of WR stars, but due to the different surface parameter values in these models as compared to those in the Padova tracks. Both the single and binary BPASS models predict systematically a smaller number of WR stars, and a lower peak value of I(He II λ4686)/I(Hβ) at the 3–5 Myr age. In binary models, peak

Table 1. Comparison of population synthesis model results for $Z = 0.008$ with observations of SSC-A.

SSP code ID	WR model + atmosphere	I(He II)/Hβ		WR phase		EW(Hβ)	Q(H0)	Comments
		age Myr	peak log	age Myr	N_{WR}	Å	log ph s^{-1}	
(1)	(2)	(3)	(4)	(5)	(6)	(7)	(8)	(9)
SB99/Padova	Padova1994+CMFGEN	3.5	−1.20	3.3–4.9	123	278–88	52.03	Good fit
SB99/Geneva	Geneva1994+CMFGEN	5.3	−2.45	3.2–4.4	155	157–85	51.98	I(He II)/I(Hβ) too low
PopStar/Padova	Padova1994+CMFGEN	4.0	−1.61	3.5–4.5	106	165–84	51.95	Good fit
BC03/Padova	Padova1994+POWR	4.0	−1.03	–	–	–	52.13	Good fit
C&B/Padova	Padova2015+POWR	4.2	−2.10	3.3–4.2	89	–	52.10	Marginal fit
BPASS/single	Cambridge+POWR	3.2	−4.03	4.0–5.0	80	180–110	52.02	I(He II)/I(Hβ) too low
BPASS/binary	Cambridge+POWR	16	−2.89	4.0–16	124	195–19	52.08	I(He II)/I(Hβ) too low
SSC-A	Observed or inferred	–	−1.69	4.0 ± 0.5	124 56–186	75 160	52.00	$(5.5 \pm 0.5) \times 10^5$ M$_\odot$

Notes. (1)–(2): Model name, evolutionary tracks, and WR atmospheric models used (Padova1994=Bressan et al. 1994; Geneva1994=Meynet et al. 1994; Padova2015=Chen et al. 2015). The last row contains observationally inferred quantities. The tracks used in PopStar are a modified version of Padova1994 tracks as described in Mollá, García-Vargas & Bressan (2009); (3) age at which nebular I(He II λ4686)/I(Hβ) ratio is maximum; (4) maximum value of I(He II λ4686)/I(Hβ) in the model in log units; (5) the age interval over which the model has more than the observationally estimated minimum number of 56 WR stars, for the determined mass. The last row contains the age range over which models using Padova tracks reproduce the observed I(He II λ4686)/I(Hβ); (6) the maximum number of WR stars in the model in the WR phase. The last row contains the best estimation and the possible range depending on the assumption on extinction; (7) range of EW(Hβ) for the age range in column 5. EW(Hβ) decreases monotonically with age. Observed range in the last row corresponds to the minimum and maximum values based on different assumptions on differential extinction (see the text for details); (8) model log[Q(H^0)] at the most likely age (4 Myr) and mass (5.5×10^5 M$_\odot$); (9) comments on the comparison between the observations and model. The last row contains the best determined mass and error on it, which takes into account the error on the determined age.

values of these two parameters are reached at later ages ($\sim$16 Myr) when Q(H^0) falls by a factor of 30 with respect to its values at the WR phase in single star evolutionary models. The observed EW of Hβ is not in favour of this advanced age.

In the right-hand panel of Fig. 9, we plot the typical emergent spectrum around the He$^+$ ionization edge (228 Å; the dashed vertical line) during the WR phase (4 Myr for all models except BPASS where it is 3.2 Myr) for a range of metallicities. All spectra are normalized to their fluxes at λ=900 Å. The normalization wavelength is specifically chosen to be slightly blueward of the H^0 ionization edge (912 Å), so that the shape of the plotted spectra blueward of 228 Å is an indicator of the I(He II λ4686)/I(Hβ) ratio. The spectra in the four models incorporating the Padova tracks (SB99/Padova, PopStar, BC03, and C&B) exhibit more He$^+$ ionizing photons blueward of 228 Å for metallicities $Z \geq 0.004$ than those in the SB99/Geneva and BPASS models. At these metallicities, the emergent spectrum using the new Padova tracks (C&B/Padova) is softer than that using the older Padova tracks, but it is still harder than that obtained in the SB99/Geneva and BPASS models. On the other hand, the spectral behaviour is similar in all the seven plotted models at low metallicities ($Z \leq 0.001$), all models predicting a downward jump at 228 Å. The plot illustrates that the atmospheric parameters (effective temperature and bolometric luminosity) of WR stars in Padova tracks are particularly able to account for the observed ratio of I(He II λ4686)/I(Hβ) at metallicities of $Z \geq 0.004$.

In the above analysis, we have compared the values of NGC 1569 with $Z = 0.008$ metallicity models. For the observed gas-phase abundance of oxygen, the metallicity Z can be as low as $Z = 0.004$ if less than 10 per cent of oxygen is depleted on to dust grains (Gutkin et al. 2016). Given that the hardness of the spectrum blueward of the He$^+$ ionization edge depends on metallicity, we now examine the behaviour of the I(He II λ4686)/I(Hβ) ratio with metallicity during the WR phase. This is illustrated in Fig. 10 for all the models discussed in this work. The observed ratio in NGC 1569 is well reproduced for a metallicity range of $Z = 0.004$–0.008 in all SSPs that use Padova tracks, independent of whether CMFGEN or POWR models

are used to represent the atmospheres of WR stars. In comparison, SSP models using Geneva tracks and BPASS models predict more than an order of magnitude lower values.

It can be seen in Fig. 10 that the I(He II λ4686)/I(Hβ) ratio decreases sharply at $Z<0.004$ in models using Padova tracks. The maximum I(He II λ4686)/I(Hβ) ratio at the lowest plotted metallicity (Z=0.0004) corresponds to the BPASS/binary model. However, the ratio just about reaches 0.01. The observed ratio in metal-poor galaxies is often higher that these predicted values (see Shirazi & Brinchmann 2012). In fact, observed data show a gradual tendency for the nebular I(He II λ4686)/I(Hβ) ratio to increase with decreasing metallicity reaching values as high as $\sim$0.06 in the most metal-poor galaxies known (Schaerer et al. 2019). This incapability of the SSP models to reproduce the observed I(He II λ4686)/I(Hβ) ratio at low metallicities ($Z < 0.004$) is often referred to as the He$^+$ ionization budget problem. The problem starts arising just below the metallicity of NGC 1569. At these low metallicities, the problem is aggravated due to the small number of WR detections. For example, I Zw 18, one of the most metal-poor galaxies, emits as much He$^+$ ionizing photons as SSC-A in NGC 1569, but it has at the most 9 WR stars detected (Kehrig et al. 2015) as compared to the 124 WR stars in SSC-A. A comprehensive analysis of this problem was carried out recently by Plat et al. (2019). They used the same C&B/Padova model that we have used here, and calculated the I(He II λ4686)/I(Hβ) ratio for a variety of additional input physics not explored in this study. They find that the conditions most favourable to produce I(He II λ4686)/I(Hβ)>0.01 at low metallicities include: (1) the presence of stars significantly more massive than 100 M$_\odot$, (2) extremely high ionization parameter, log (U) > −1, (3) the presence of interacting binaries that produce X-rays, (4) ionization of He$^+$ by radiative shocks, or (5) when analysing integrated spectra of distant galaxies, ionization of He$^+$ by an active galactic nucleus. It is likely that more than one of these conditions are met in some of the metal-poor galaxies.

In summary, the observed number of Q(H^0) from nebula surrounding SSC-A and N_{WR} in SSC-A are consistent with each other
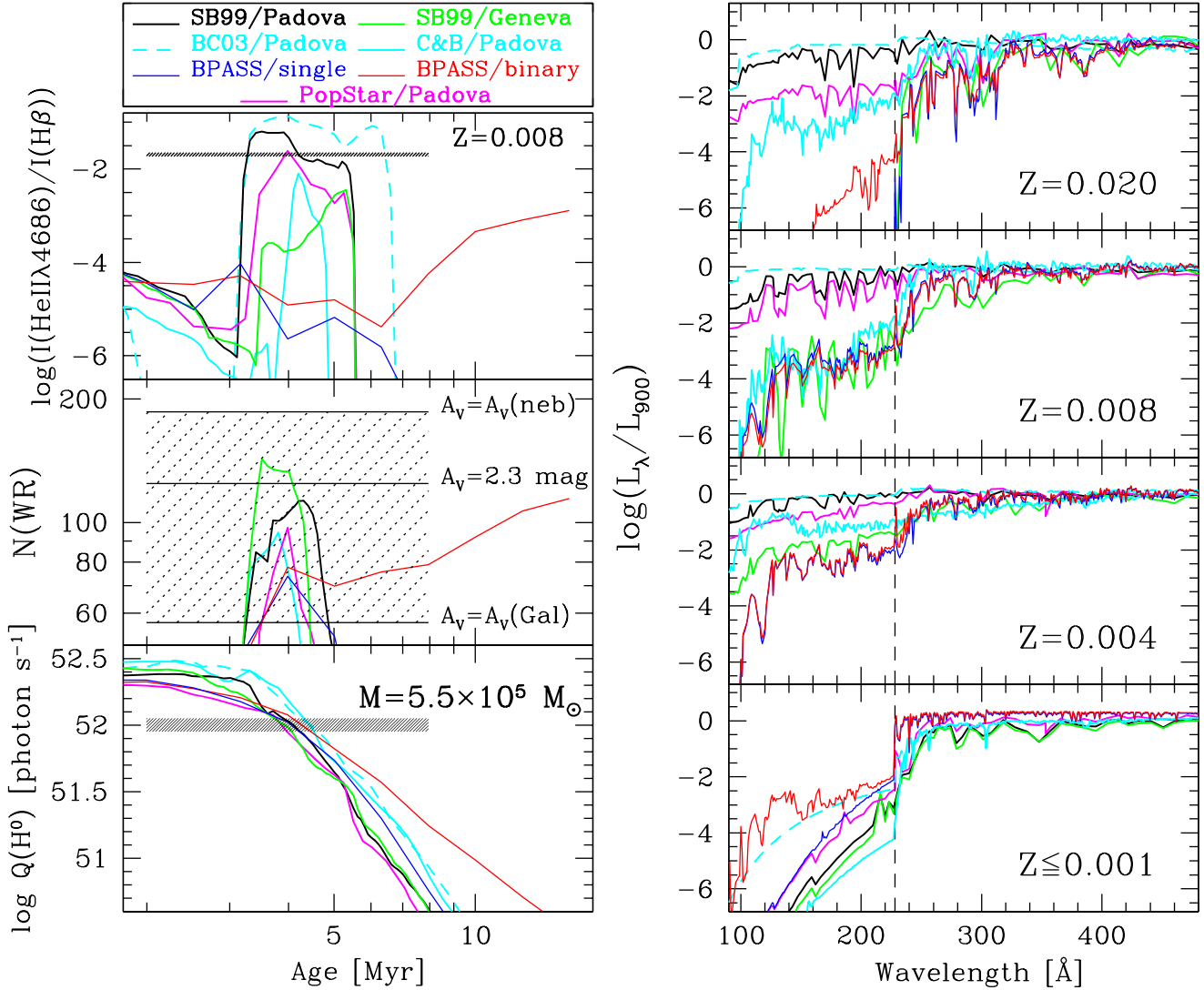
Figure 9. (Left-hand panels) Comparison of observed quantities in NGC 1569 with population synthesis models. The plotted observed quantities (horizontal hatched areas) are the ratio of integrated nebular He II λ4686 line flux to that of H β line (top-left), the number of WR stars in SSC-A (middle-left), and the rate of hydrogen ionizing photons determined from the integrated H β flux (bottom-left). Results from seven different population synthesis models are shown, which are identified in a box above the plots (see the text and Table 1 for details of these models). Models that use Padova evolutionary tracks are able to reproduce the observed values for a cluster of mass =5.5 × 10⁵ M$_\odot$ at an age of 4 Myr. All models use Kroupa IMF at Z = 0.008, which is the metallicity closest to that of NGC 1569 available in all the codes. (Right-hand panels) Spectral shape near the He$^+$ ionizing edge (228 Å) at the four indicated metallicities during the WR phase. Spectra are shown normalized to their flux at 900 Å wavelength. All spectra show a jump blueward of 228 Å at the lowest plotted metallicity. However, at higher metallicities the spectral shapes blueward of 228 Å for the plotted models do not coincide, with the spectra being harder in models incorporating Padova tracks as compared to those obtained using other tracks.

for all models for a cluster mass of (5.5 ± 0.5) × 10⁵ M$_\odot$ at ~4.0 ± 0.5 Myr age. The observed nebular I(He II λ4686)/I(H β) ratio is in the range of predicted values during the WR phase in models that use Padova evolutionary tracks. The inferred age for SSC-A is in agreement with the age of 4.5 Myr determined by Larsen et al. (2011) using the CMD of stars in the periphery of SSC-A. The inferred mass is ~15 per cent lower as compared to the photometric mass of 6.3 × 10⁵ M$_\odot$ determined by Larsen et al. (2011), after scaling their mass to the distance of 3.1 Mpc used in this work. Slightly larger mass for SSC-A in Larsen et al. (2011) is expected given that the SSC-A has two populations, a centrally concentrated population (A1) containing RSGs (older than 7 Myr) and a slightly extended component (A2) containing WR and O

stars. Our measured mass is based on the ionizing flux and hence corresponds to the mass of the component A2. On the other hand, the photometric mass derived by Larsen et al. (2011) is based on integrated photometry of stellar light, and hence it includes the mass of both the components. On the other hand, the mass derived by us is ~25 per cent higher than the dynamical mass of 4.1 × 10⁵ M$_\odot$ obtained by Ho & Filippenko (1996) using spectral lines originating in cool supergiants. Ho & Filippenko (1996) commented that the velocity dispersion obtained from cool supergiants in the integrated spectrum could underestimate the mass by as much as a factor of 2. Furthermore, the cool supergiants belong to the older of the two populations. The derived dynamical mass is expected to be the total of the two populations if they are dynamically mixed. The presence of
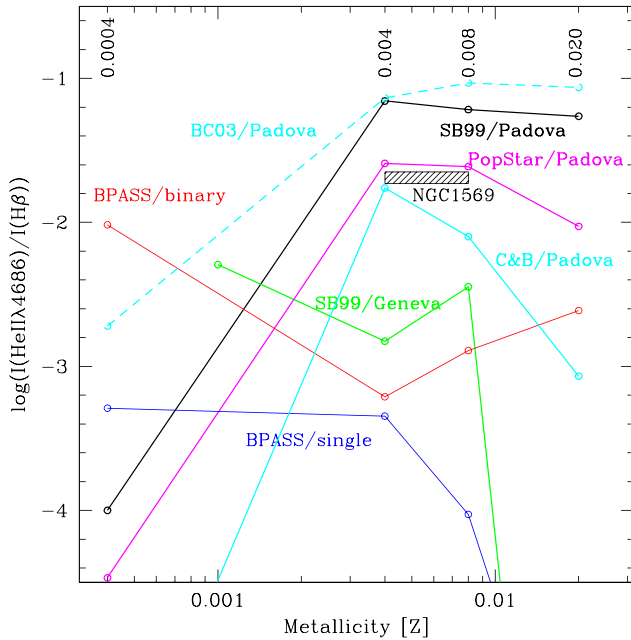
Figure 10. Maximum values of the nebular $I(\text{He\,II}\,\lambda4686)/I(\text{H}\beta)$ ratio (points joined by lines) reached as a function of the abundance for the SSP models indicated close to each curve. The observed value for NGC 1569 is indicated, where the range in metallicity takes into account 10–30 per cent depletion of oxygen into dust grains (Gutkin et al. 2016). The observed values are in agreement with the highest values of model $I(\text{He\,II}\,\lambda4686)/I(\text{H}\beta)$ ratio, which happens between $Z = 0.004$ and 0.008 for new (C&B/Padova) as well as old Padova (SB99/Padova, PopStar/Padova) models.

hot massive stars, but not cool supergiants, in the periphery of SSC-A argues against such a mixing (Larsen et al. 2011). Measurements of velocity dispersion using spectral lines sensitive to hot stars (e.g. He absorption lines that are prominent in the spectrum of SSC-A) could help us to address this issue. MEGARA has the capability of obtaining velocity dispersion in its high-resolution mode, providing a possibility of addressing this issue in the near future.

5.2 Morphology of the He II λ4686 nebula and the location of SSC-A

We found that the entire observed He II λ4686 emission can be understood in terms of the ionization from WR stars in SSC-A. However, the observed He II λ4686 emission is not coincident with the location of the ionizing cluster. Instead, the most intense part of the ionized nebula in both the Balmer and He II λ4686 lines lies ∼40 pc to the south-west of the cluster. The zone of intense emission is part of a semicircular arc of 150 pc diameter, with its centre ∼40 pc to the east of SSC-A. Because of this off-centring, the distance of ionizing source to different parts of the emitting arc is different, causing the surface brightness of the emission to decrease along the arc as its distance increases from SSC-A. The emission is weak inside the semicircular arc (see Section 3). The observed morphology resembles the structure of a classical wind-driven bubble. If this is the case, the hot shocked gas that fills the bubble should be a source of the X-ray emission (Weaver et al. 1977; Chu & Mac Low 1990; Silich et al. 2005). Soft X-rays are indeed detected in NGC 1569, whose morphology is discussed below.

5.3 X-ray morphology

The combined effect of stellar winds from massive stars in cluster A, including those from the multiple WR stars, is to form a global star cluster wind able to expel the inserted and the residual gas away into the interstellar medium (ISM). The interaction of the combined star cluster wind with the ISM leads to a strong shock that sweeps up the ambient gas into a thin shell, while the cluster wind is thermalized at a reverse shock. The shell of swept-up matter cools rapidly, if the ambient gas density is not too small, to be then completely or partially photoionized by the energetic photons escaping the cluster (Castor, McCray & Weaver 1975; Martínez-González, Silich & Tenorio-Tagle 2014).

Both soft (0.2–2 keV) and hard (2–10 keV) X-ray emissions have been detected from the central zone of NGC 1569 (Martin et al. 2002; Sánchez-Cruces et al. 2015). The soft X-ray emission is diffuse, whereas the hard X-rays principally come from point sources. We plot the X-ray map (blue) superposed on the He II nebular map (green) in Fig. 11. The F658N image (Hα + continuum emission) is shown in red for positional reference. The observed FoV contains two hard X-ray-emitting point sources catalogued by Sánchez-Cruces et al. (2015): Source 27 (identified as X27) is associated with an X-ray binary, and source 33 (denoted as X33) as originating in the cluster 29 of Hunter et al. (2000) (see our Fig. 3).

Most of the soft X-ray emission comes from diffuse regions coincident with parts of the He II nebula. However, the brightest part of the He II nebula does not show any X-ray emission. As illustrated by Sánchez-Cruces et al. (2015), there is faint emission from the intervening zone between the SSC-A and the ionized nebula. This emission is likely associated with the hot shocked winds.

X-ray photons can also produce the He II emission. We used the factor $q = Q(\text{He}^+)/L_X = 2 \times 10^{10}$ photon erg^{-1} defined by Schaerer et al. (2019) to estimate the $Q(\text{He}^+)$ using the observed X-ray luminosity from the two X-ray sources in our FoV. The two sources combined contribute ∼1.7×10^{48} photon s^{-1}, which is less than 2 per cent of the observed ionization requirement. Hence, we are justified in neglecting any contribution to ionization from X-ray photons.

6 CONCLUSIONS

Using the recently available integral field spectrograph MEGARA at the 10.4 m GTC, we detect extended He II λ4686 nebula in the central starburst zone of the nearby dwarf galaxy NGC 1569. The nebula extends along a semicircular arc of ∼150 pc (10 arcsec) diameter and ∼40 pc width, with the zone of the brightest He II λ4686 nebular emission lying at ∼40 pc (2.5 arcsec) south-west of the massive young cluster SSC-A. The spectral data also show broad He II λ4686 emission from 18 individual fibres belonging to the SSC-A. None of the other sources that are well separated from SSC-A, where WR detection has been reported using *HST* imaging data by Buckalew et al. (2000), show broad He II λ4686 emission. We find that these sources are stars and clusters immersed in the He II λ4686 nebula. We use the Hβ and Hγ nebular lines in the same spectra to map the extinction in the observed zone. The minimum extinction we obtain is consistent with the $A_V = 1.6$ mag value from the Milky Way along the line of sight to NGC 1569. The mean value for all fibres where we could reliably measure A_V is $A_V = 2.65$ mag. The low surface brightness of the nebular flux in and around SSC-A prevented us from obtaining nebular extinction towards this cluster. Using $A_V = 2.3$ mag, the value used by Larsen et al. (2011) to interpret the colours of the resolved stellar population in SSC-A, we estimate 124 ± 11
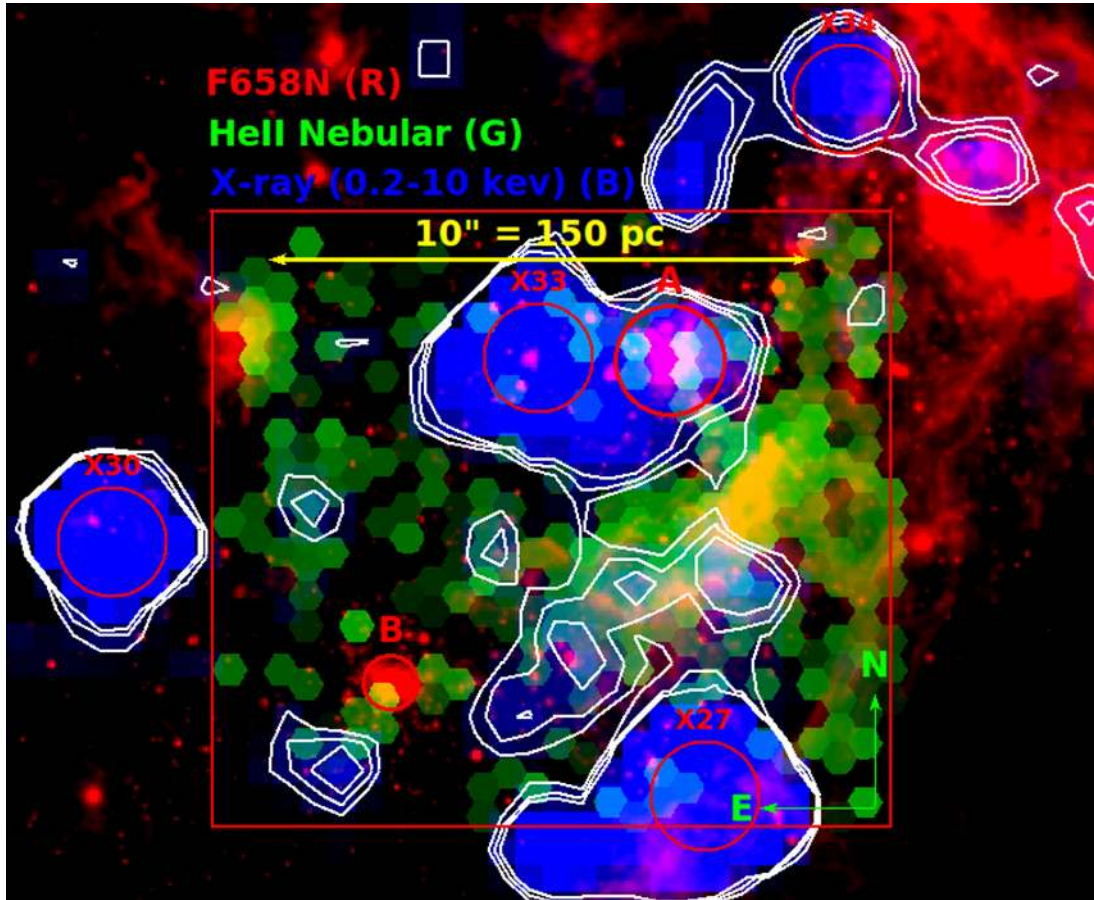
Figure 11. X-ray emission map from the *Chandra*/ACIS image (0.2–10 keV band) from Sánchez-Cruces et al. (2015) in blue is superposed on the He II nebular map in green and F658N (Hα+continuum) in red. The contours show the X-ray emission at 3 levels (3σ, 3.5σ, and 4σ above the background) to help see the position of the faint X-ray diffuse emission with respect to the He II λ4686 nebular emission. Most of the X-ray emission within the MEGARA FoV (red square) originates in two hard X-ray point sources (X27 and X33), which are marked by red circles. The diffuse X-ray emission coincides with part of the He II λ4686 nebular emission. However, there is no X-ray emission at the brightest zone of the nebular He II λ4686 emission.

WR stars of type WNL in SSC-A. We derive hydrogen and He$^+$ ionizing rates of 1×10^{52} and 1×10^{50} photon s^{-1}, respectively. These observed quantities are in agreement with the expectations from single stellar population models at 4.0 ± 0.5 Myr for a cluster of mass $(5.5 \pm 0.5) \times 10^5$ M$_\odot$. The derived age is consistent with the turn-off ages determined by Larsen et al. (2011) from resolved stellar populations in the periphery of this cluster. Through a careful comparison of the most commonly used population synthesis models, we find that the predicted values of nebular I(He II λ4686)/I(H β) in models that make use of Padova evolutionary tracks are in the range of observed value of 0.02 for metallicities $Z \geq 0.004$. Thus, at $12 + \log(O/H) = 8.19$ ($Z \sim 0.006$), which is the measured value for NGC 1569, the WR stars from the cluster are able to explain the origin of the He II λ4686 nebula.

DATA AVAILABILITY

The fluxes of principal emission lines used in this work are available in the article and in its online supplementary material. The reduced fit files on which these data are based will be shared on reasonable request to the first author.

REFERENCES

Arp H., Sandage A., 1985, AJ, 90, 1163
Bressan A., Chiosi C., Fagotto F., 1994, ApJS, 94, 63
Brinchmann J., Kunth D., Durret F., 2008, A&A, 485, 657

Bruzual A. G., Charlot S., 2003, MNRAS, 344, 1000
Buckalew B. A., Dufour R. J., Shopbell P. L., Walter D. K., 2000, AJ, 120, 2402
Burstein D., Heiles C., 1984, ApJS, 54, 33
Calzetti D., Kinney A. L., Storchi-Bergmann T., 1994, ApJ, 429, 582
Cardelli J. A., Clayton G. C., Mathis J. S., 1989, ApJ, 345, 245
Carrasco E. et al., 2018, in Christopher J. E., Luc S., Hideki T., eds., Proc. SPIE Conf. Ser. Vol. 1070216. SPIE, Bellingham, p. 10702
Castor J., McCray R., Weaver R., 1975, ApJ, 200, L107
Chen Y., Bressan A., Girardi L., Marigo P., Kong X., Lanza A., 2015, MNRAS, 452, 1068
Chu Y.-H., Mac Low M.-M., 1990, ApJ, 365, 510
De Marchi G., Clampin M., Greggio L., Leitherer C., Nota A., Tosi M., 1997, ApJ, 479, L27
Devost D., Roy J.-R., Drissen L., 1997, ApJ, 482, 765
Dopita M. A., Sutherland R. S., 1996, ApJS, 102, 161
Eldridge J. J., Stanway E. R., Xiao L., McClelland L. A. S., Taylor G., Ng M., Greis S. M. L., Bray J. C., 2017, Publ. Astron. Soc. Aust., 34, e058
Garnett D. R., Kennicutt R. C., Chu Y.-H., Skillman E. D., 1991, ApJ, 373, 458
Gil de Paz A. et al., 2018, in Christopher J. E., Luc S., Hideki T., eds., Proc. SPIE Conf. Ser. Vol. 1070217. SPIE, Bellingham, p. 10702
Gil de Paz A. et al., 2020, A&A, submitted
Gómez-González V. M. A. et al., 2020, MNRAS, 493, 3879
González-Delgado R. M., Leitherer C., Heckman T., Cerviño M., 1997, ApJ, 483, 705
Gräfener G., Koesterke L., Hamann W.-R., 2002, A&A, 387, 244
Grocholski A. J. et al., 2008, ApJ, 686, L79
Grocholski A. J., van der Marel R. P., Aloisi A., Annibali F., Greggio L., Tosi M., 2012, AJ, 143, 117
Gutkin J., Charlot S., Bruzual G., 2016, MNRAS, 462, 1757
Hillier D. J., Miller D. L., 1998, 496, 407
Ho L. C., Filippenko A. V., 1996, ApJ, 446, L83
Hodge P. W., 1974, ApJ, 191, L21
Hunter D. A., Hawley W., Gallagher J. S., 1993, AJ, 106, 1797
Hunter D. A., O'Connell R. W., Gallagher J. S., Smecker-Hane T. A., 2000, AJ, 120, 2383
Israel F. P., 1988, A&A, 194, 24
Kehrig C. et al., 2011, A&A, 526, L128
Kehrig C., Vílchez J. M., Pérez-Montero E., Iglesias-Páramo J., Brinchmann J., Kunth D., Durret F., Bayo F. M., 2015, ApJ, 80, L28
Kehrig C., Vílchez J. M., Guerrero M. A., Iglesias-Páramo J., Hunt L. K., Duarte-Puertas S., Ramos-Larios G., 2018, MNRAS, 480, 1081
Kobulnicky H. A., Skillman E. D., 1997, ApJ, 489, 636
Kojima T. et al., 2020, preprint(arXiv:2006.03831)
Kroupa P., 2001, MNRAS, 322, 231
Larsen S. S., Origlia L., Brodie J., Gallagher J. S., 2008, MNRAS, 383, 263
Larsen S. S. et al., 2011, A&A, 532, 147
Leitherer C. et al., 1999, ApJ, 123, 3
Leitherer C., Ekström S., Meynet G., Schaerer D., Agienko K. B., Levesque E. M., 2014, ApJS, 212, 14
López-Sánchez Á. R., Esteban C., 2010, A&A, 516, A104
Maeder A., Meynet G., 1989, A&A, 210, 155
Martínez-González S., Silich S., Tenorio-Tagle G., 2014, ApJ, 785, 164
Martin C. L., Kobulniky H. A., Heckman T. M., 2002, ApJ, 574, 663
Mayya Y. D., Prabhu T. P., 1996, AJ, 111, 1252
Meynet G., Maeder A., 2005, A&A, 429, 581
Meynet G., Maeder A., Schaller G., Schaerer D., Charbonnel C., 1994, A&AS, 103, 97
Mollá M., García-Vargas M. L., Bressan A., 2009, MNRAS, 398, 451
Origlia L., Leitherer C., Aloisi A., Greggio L., Tosi M., 2001, AJ, 122, 815
Osterbrock D. E., Ferland G. J., 2006, Astrophysics of Gaseous Nebulae and Active Galactic Nuclei. Univ. Sci. Books, CA, USA
Ott T., 2012, QFitsView: FITS File Viewer, Astrophysics Source Code Library, record ascl:1210.019
Pascual S., Cardiel N., Picazo-Sanchez P., Castillo-Morales A., Gil de Paz A., 2018, guaix-ucm/megaradrp: v0.8. available at: https://zenodo.org/record/2206856
Pauldrach A. W. A., Hoffmann T. L., Lennon M., 2001, A&A, 375, 161
Plat A., Charlot S., Bruzual G., Feltre A., Vidal-García A., Morisset C., Chevallard J., Todt H., 2019, MNRAS, 490, 978
Prada F., Greve A., McKeith C. D., 1994, A&A, 288, 396
Press W. H., Teukolsky S. A., Vetterling W. T., Flannery B. P., 1992, Numerical Recipes in C, 2nd edn. Cambridge Univ. Press, Cambridge
Sánchez-Cruces M., Rosado M., Rodríguez-González A., Reyes-Iturbide J., 2015, ApJ, 799, 231
Schaerer D., Fragos T., Izotov Y. I., 2019, A&A, 622, L10
Schaerer D., 1996, ApJ, 467, L17
Schaller G., Schaerer, G. Meynet G., Maeder A., 1992, A&AS, 96, 269
Schlafly E., Finkbeiner D. P., 2011, ApJ, 737, 103
Schlegel D. J., Finkbeiner D. P., Davis M., 1998, ApJ, 500, 525
Schmutz W., Leitherer C., Gruenwald R., 1992, PASP, 104, 1164
Shirazi M., Brinchmann J., 2012, MNRAS, 421, 1043
Silich S., Tenorio-Tagle G., Añorve-Zeferino G. A., 2005, ApJ, 635, 1116
Smith L., Norris R., Crowther P., 2002, MNRAS, 337, 1309
Taylor C. L., Hüttemeister S., Klein U., Greve A., 1999, A&A, 349, 424
Tresse L., Maddox S., Loveday J., Singleton C., 1999, MNRAS, 310, 262
Vacca W. D., Conti P. S., 1992, ApJ, 401, 543
Waller W. H., 1991, ApJ, 370, 144
Weaver R., McCray R., Castor J., Shapiro P., Moore R., 1977, ApJ, 218, 377
Westmoquette M. S., Exter K. M., Smith L. J., Gallagher J. S., 2007, MNRAS, 381, 894
Westmoquette M. S., Smith L. J., Gallagher J. S., 2008, MNRAS, 383, 864
Xiao L., Stanway E. R., Eldridge J. J., 2018, MNRAS, 477, 904

SUPPORTING INFORMATION

Supplementary data are available at *MNRAS* online.

ngc1569_paper_table.dat

Please note: Oxford University Press is not responsible for the content or functionality of any supporting materials supplied by the authors. Any queries (other than missing material) should be directed to the corresponding author for the article.

APPENDIX A: MEASURED DATA IN INDIVIDUAL FIBRE SPECTRUM

In Table A1, we give the measured and calculated values for all the lines used in this work for 50 illustrative fibre spectra. The first 25 rows contain data for fibres arranged as a decreasing function of H β flux (column 6), whereas the remaining 25 rows show data for fibres where we detected WR features. These data are arranged in the decreasing order of N_{WR} (column 19). The electronic version contains data for all the 567 fibres, arranged in the increasing order of fibre number (column 1). The note to the table contains a detailed explanation of the quantities in each column. In Fig. A1, we show a spaxel map of MEGARA, where we indicate the location of each fibre, identified by its number.

Table A1. He II λ4686 nebular and WR parameters measured in individual fibre spectra.

	Fibre coordinates					Hβ-related			Hγ-related		He II λ4686 nebula-related					He II λ4686 WR-related				Extinction	
Fno	dX	dY	R	PA	f_T	SNR	EW	FW	fβ	SNR	$λ_0$	FW	f_T	SNR	fβ	$λ_0$	FW	N_{WR}	eN	A_V	eA_V
	arcsec	arcsec	pc	°			Å	Å			Å	Å				Å	Å			mag	mag
1	2	3	4	5	6	7	8	9	10	11	12	13	14	15	16	17	18	19	20	21	22
242	1.86	−1.61	36.9	229.1	6.181	82.7	51.2	1.2	19.6	10.8	4685.1	4.1	10.230	8.8	3.7	0.0	0.0	0.0	0.0	4.52	0.43
240	2.32	−1.34	40.3	240.0	3.990	56.2	41.1	1.3	19.6	9.1	4684.7	2.5	8.726	10.7	4.9	0.0	0.0	0.0	0.0	4.40	0.48
244	2.32	−1.88	44.9	231.0	3.972	59.9	57.1	1.2	21.8	9.6	4684.9	2.9	6.808	9.6	3.8	0.0	0.0	0.0	0.0	4.12	0.48
246	1.86	−2.15	42.7	220.8	3.010	70.5	64.5	1.2	23.4	16.7	4684.8	2.1	4.168	10.3	3.1	0.0	0.0	0.0	0.0	3.65	0.25
406	0.46	−4.03	60.9	186.6	2.171	67.0	50.5	1.3	23.0	14.1	4685.1	2.1	2.881	9.2	2.9	0.0	0.0	0.0	0.0	3.71	0.30
20	−7.89	0.81	119.2	84.2	2.144	63.4	41.1	1.4	24.2	10.4	4684.8	1.4	1.503	4.8	1.6	0.0	0.0	0.0	0.0	3.57	0.45
248	2.32	−2.42	50.4	223.8	2.140	73.2	61.0	1.2	23.4	13.0	4684.7	1.6	2.257	8.6	2.3	0.0	0.0	0.0	0.0	3.58	0.34
256	2.79	−1.61	48.4	240.0	1.867	61.4	39.4	1.4	21.8	8.9	4685.1	2.4	3.300	7.5	3.9	0.0	0.0	0.0	0.0	3.85	0.51
250	1.86	−2.68	49.1	214.7	1.791	79.6	68.2	1.2	25.3	12.8	4684.8	1.7	1.621	7.4	2.0	0.0	0.0	0.0	0.0	3.20	0.36
234	1.39	−2.42	41.9	210.0	1.667	80.9	59.2	1.3	25.6	15.2	4684.7	2.0	2.191	10.9	2.9	0.0	0.0	0.0	0.0	3.19	0.29
260	2.79	−2.15	52.9	232.4	1.450	51.2	44.5	1.4	23.4	9.4	4684.6	2.4	1.845	6.0	2.8	0.0	0.0	0.0	0.0	3.55	0.46
238	1.39	−2.95	49.1	205.2	1.290	87.0	61.5	1.3	26.8	16.4	4685.0	2.5	1.594	9.4	2.7	0.0	0.0	0.0	0.0	2.93	0.27
230	1.39	−1.88	35.2	216.5	1.088	67.2	42.1	1.3	26.0	13.6	4684.8	2.8	2.052	11.3	4.2	0.0	0.0	0.0	0.0	3.03	0.32
497	3.25	−0.27	49.0	265.3	1.033	49.4	28.6	1.8	23.4	10.7	0.0	0.0	0.000	0.0	0.0	0.0	0.0	0.0	0.0	3.46	0.39
468	1.86	−1.07	32.2	240.0	0.997	49.7	26.3	1.5	24.2	9.3	4685.1	2.6	1.294	5.4	2.9	0.0	0.0	0.0	0.0	3.31	0.47
372	1.86	−3.22	55.9	210.0	0.986	64.6	60.4	1.2	27.3	20.6	4684.8	1.7	0.915	10.4	2.1	0.0	0.0	0.0	0.0	2.79	0.18
374	2.32	−3.49	63.0	213.6	0.946	54.0	50.0	1.2	25.4	11.9	4684.3	0.8	0.239	2.3	0.6	0.0	0.0	0.0	0.0	3.18	0.36
404	0.31	−3.76	56.5	184.7	0.904	58.2	35.1	1.3	24.9	9.5	4685.1	2.3	1.542	9.0	3.8	0.0	0.0	0.0	0.0	3.20	0.47
358	2.79	−3.22	64.0	220.8	0.896	47.0	47.2	1.2	25.2	9.0	4684.8	2.3	0.850	4.8	2.1	0.0	0.0	0.0	0.0	3.21	0.49
513	3.71	−0.54	56.4	261.8	0.869	51.4	26.4	1.7	23.9	8.8	0.0	0.0	0.000	0.0	0.0	0.0	0.0	0.0	0.0	3.26	0.49
615	0.31	−8.59	129.1	182.1	0.846	55.7	78.0	1.3	28.0	8.8	0.0	0.0	0.000	0.0	0.0	0.0	0.0	0.0	0.0	2.77	0.53
236	0.93	−2.68	42.7	199.1	0.843	70.3	44.7	1.4	27.2	15.2	4684.8	2.5	1.393	11.8	3.7	0.0	0.0	0.0	0.0	2.80	0.28
264	2.79	−2.68	58.1	226.1	0.843	44.6	44.2	1.2	25.2	11.0	4685.0	1.5	0.775	5.0	2.0	0.0	0.0	0.0	0.0	3.05	0.36
232	0.93	−2.15	35.2	203.4	0.832	70.3	29.7	1.5	24.9	9.5	4684.8	1.1	0.584	4.4	1.6	4685.0	8.2	0.7	0.1	3.08	0.48
390	0.93	−3.76	58.2	193.9	0.773	77.1	48.8	1.4	27.5	15.1	4685.2	2.0	0.822	8.7	2.4	0.0	0.0	0.0	0.0	2.76	0.29
418	0.31	0.31	4.7	135.0	0.175	32.0	2.3	2.5	18.9	5.4	0.0	0.0	0.000	0.0	0.0	4685.5	28.8	19.8	0.8	1.06	0.43
416	0.46	0.27	8.1	120.0	0.158	31.1	1.9	2.1	22.5	6.3	4685.1	2.5	0.413	3.4	5.8	4685.7	27.5	14.8	0.8	1.75	0.48
420	0.46	−0.27	8.1	240.0	0.142	45.0	2.2	2.2	18.4	4.6	4684.5	1.7	0.326	3.3	5.1	4686.3	25.6	13.3	0.8	1.10	0.54
414	0.31	0.54	8.1	150.0	0.107	33.6	2.1	2.1	22.7	5.8	0.0	0.0	0.000	0.0	0.0	4686.6	29.8	12.6	0.6	1.44	0.51
419	−7.43	0.31	111.6	87.6	0.240	58.5	11.2	1.4	22.2	14.6	4685.0	2.2	0.393	5.3	3.6	4685.3	73.1	11.2	0.6	1.87	0.19
422	0.31	−0.54	8.1	210.0	0.098	37.2	2.6	2.3	24.7	5.4	0.0	0.0	0.000	0.0	0.0	4685.7	24.9	10.0	0.5	0.00	0.43
144	−0.46	0.27	8.1	60.0	0.065	29.6	2.0	2.4	3.7	1.3	4684.5	4.2	0.363	4.5	12.5	4685.4	38.7	8.3	0.5	0.00	0.00
446	0.93	0.31	14.0	108.5	0.117	37.4	2.9	1.9	18.8	5.9	4685.5	1.2	0.111	2.4	2.1	4686.7	30.0	7.2	0.5	2.50	0.51
21	0.46	0.81	14.0	150.0	0.141	47.9	3.4	2.2	17.2	6.7	0.0	0.0	0.000	0.0	0.0	4686.5	24.5	6.9	0.5	3.38	0.49
148	−0.46	−0.27	8.1	120.0	0.059	24.6	2.0	2.4	21.4	3.2	4683.9	1.6	0.129	2.4	4.9	4685.9	26.6	6.5	0.4	0.00	0.65
424	0.46	−0.81	14.0	210.0	0.085	35.7	4.1	1.9	33.5	8.5	4684.7	2.1	0.114	2.4	3.0	4687.1	25.6	4.4	0.3	0.00	0.35
442	0.93	0.54	16.1	120.0	0.105	39.6	3.4	2.0	18.4	6.2	4685.4	1.4	0.112	2.5	2.4	4685.8	24.1	4.4	0.4	3.36	0.55
145	−2.79	0.31	41.9	83.6	0.025	15.7	2.1	2.0	4.7	0.8	0.0	0.0	0.000	0.0	0.0	4685.0	28.6	3.6	0.3	0.00	0.00
152	−0.46	−0.81	14.0	150.0	0.034	14.1	2.2	2.3	7.9	1.7	0.0	0.0	0.000	0.0	0.0	4684.4	30.5	3.2	0.4	0.00	0.00
146	−0.93	0.31	14.0	71.5	0.028	12.8	1.9	2.0	3.1	0.7	0.0	0.0	0.000	0.0	0.0	4686.4	27.2	3.0	0.3	0.00	0.00
531	−0.46	0.81	14.0	30.0	0.051	33.5	2.5	1.9	13.7	3.2	4684.9	1.1	0.076	2.4	3.3	4688.7	23.1	2.9	0.3	1.85	0.66
149	−2.79	−0.54	42.6	100.9	0.019	12.9	1.8	2.0	9.5	1.1	4688.2	2.1	0.082	0.0	9.6	4685.8	27.8	2.6	0.3	0.00	0.00
423	−7.43	−0.54	111.9	94.1	0.118	44.3	10.8	1.5	24.8	7.1	4684.7	1.2	0.087	2.3	1.6	4685.6	25.8	2.5	0.4	0.48	0.39
19	0.31	1.07	16.1	163.9	0.106	40.9	4.4	2.5	18.9	4.8	4685.2	0.7	0.071	2.2	1.5	4687.9	15.2	2.3	0.3	3.14	0.74
417	−7.89	0.27	118.7	88.1	0.221	71.5	12.8	1.3	23.1	12.1	0.0	0.0	0.000	0.0	0.0	4684.5	10.7	2.1	0.2	1.51	0.25
51	−6.03	1.34	92.9	77.5	0.067	32.3	14.8	1.9	29.8	4.5	4684.5	1.7	0.084	2.4	2.8	4688.6	38.4	2.0	0.3	1.75	0.96
448	1.39	−0.27	21.3	259.1	0.109	42.1	8.1	1.7	27.5	7.3	0.0	0.0	0.000	0.0	0.0	4689.4	25.0	1.8	0.3	1.91	0.54

Table A1 – *continued*

Fno	Fibre coordinates					Hβ-related			Hγ-related		He II λ4686 nebula-related					He II λ4686 WR-related				Extinction	
	dX	dY	R	PA	f_T	SNR	EW	FW	fβ	SNR	λ_0	FW	f_T	SNR	fβ	λ_0	FW	N_{WR}	eN	A_V	eA_V
	arcsec	arcsec	pc	°			Å	Å			Å	Å				Å	Å			mag	mag
1	2	3	4	5	6	7	8	9	10	11	12	13	14	15	16	17	18	19	20	21	22
452	1.39	−0.81	24.2	240.0	0.335	49.2	12.2	1.7	25.6	9.4	0.0	0.0	0.000	0.0	0.0	4688.4	20.1	1.8	0.2	2.58	0.43
212	0.46	−1.34	21.3	199.1	0.062	28.5	7.0	1.8	37.2	6.3	0.0	0.0	0.000	0.0	0.0	4685.4	19.5	1.5	0.2	0.04	0.57
49	−5.57	1.61	87.1	73.9	0.052	28.4	11.6	2.0	31.8	3.8	4685.4	0.9	0.056	2.6	2.4	4686.1	32.7	1.4	0.3	1.63	1.18

Notes. Row description:

Data for 50 fibres, ordered according to the decreasing contribution in H β (column 6) in the first 25 rows, and ordered according to the decreasing number of WR stars (column 19) in the next 25 lines. Table containing data for all 567 fibres (excluding the sky fibres) is available in the electronic version.

Column description:

1 - Fibre number.

2–3 - X and Y shifts in arcsec with respect to (wrt) the core of SSC-A, which is the closest to fibre #418. Objects to the east and south of SSC-A have negative shifts.

4 - Distance from SSC-A in parsec using a scale of 15 pc arcsec^{-1}.

5 - PA in degrees of the fibre position wrt SSC-A.

6 - 100× the extinction-corrected H β flux in the fibre wrt total H β flux (4.444×10^{-12} erg cm^{-2} s^{-1}).

7 - SNR of the H β line (see equation 1).

8 - Emission EW in Å of the H β emission line.

9 - FWHM in Å of the fitted Gaussian to the emission line of H β.

10 - 100× $\frac{f_{H\gamma}}{f_{H\beta}}$ ratio.

11 - SNR of the H γ emission line.

12 - Central wavelength in Å of the fitted He II λ4686 narrow (nebular) line.

13 - FWHM in Å of the fitted He II λ4686 narrow (nebular) line.

14 - 100× the extinction-corrected He II λ4686 nebular line flux in the fibre wrt total flux in the same line (9.13×10^{-14} erg cm^{-2} s^{-1}).

15 - SNR of the fitted He II λ4686 narrow (nebular) line.

16 - 100× $\frac{f_{He\,II\lambda4686(nebular)}}{f_{H\beta}}$ ratio.

17 - Central wavelength in Å of the fitted He II λ4686 broad (WR) line.

18 - FWHM in Å of the fitted He II λ4686 broad (WR) line.

19 - Luminosity of the He II λ4686 broad line expressed in units of 1.22×10^{36} erg s^{-1} ≡ N_{WR} = equivalent number of WNL stars.

20 - Error in N_{WR}, determined by propagating errors in the He II λ4686 broad line flux.

21 - A_V determined from the H γ and H β lines when both the lines have SNR > 3 (absorption correction 1 Å in EWs.)

22 - Error on A_V, determined by propagating errors in the H β and H γ line fluxes.
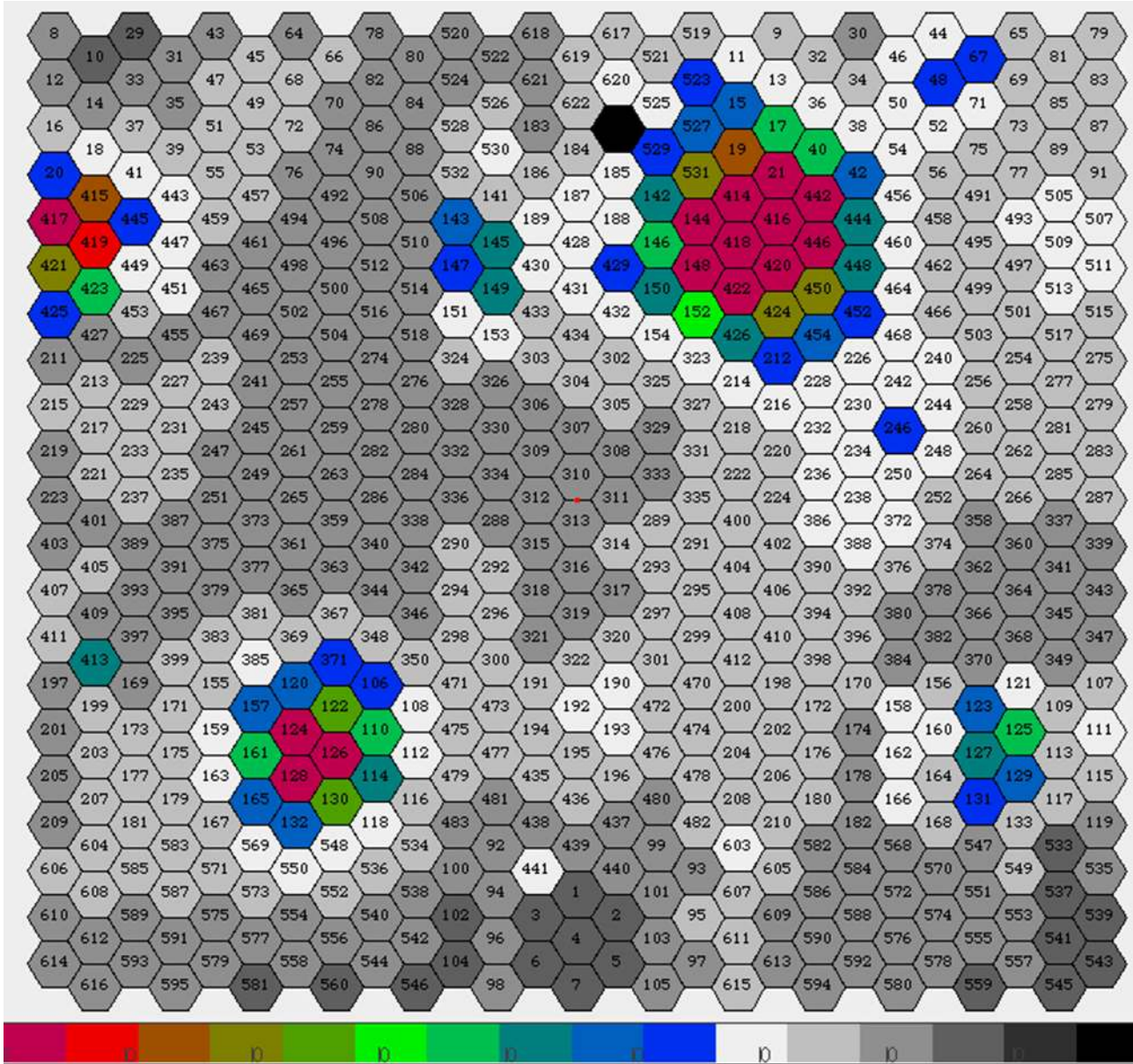
Figure A1. Spaxel (hexagon) map of the region of NGC 1569 observed by MEGARA. The spaxel contains the summed flux from the entire spectra. The colour scale at the bottom: the black colour indicates faint regions and the red the brightest regions. The numbers indicate the fibre identification numbers. The fibres nearest to the centres of SSC-A and SSC-B are #418 and 128, respectively. All coloured hexagons in the same rows but to the left of SSC-A, and to the right of SSC-B are artefacts due to the cross-talk with the fibres pointed to these two bright clusters, respectively.

This paper has been typeset from a TEX/LATEX file prepared by the author.